CHALMERS
UNIVERSITY OF TECHNOLOGY

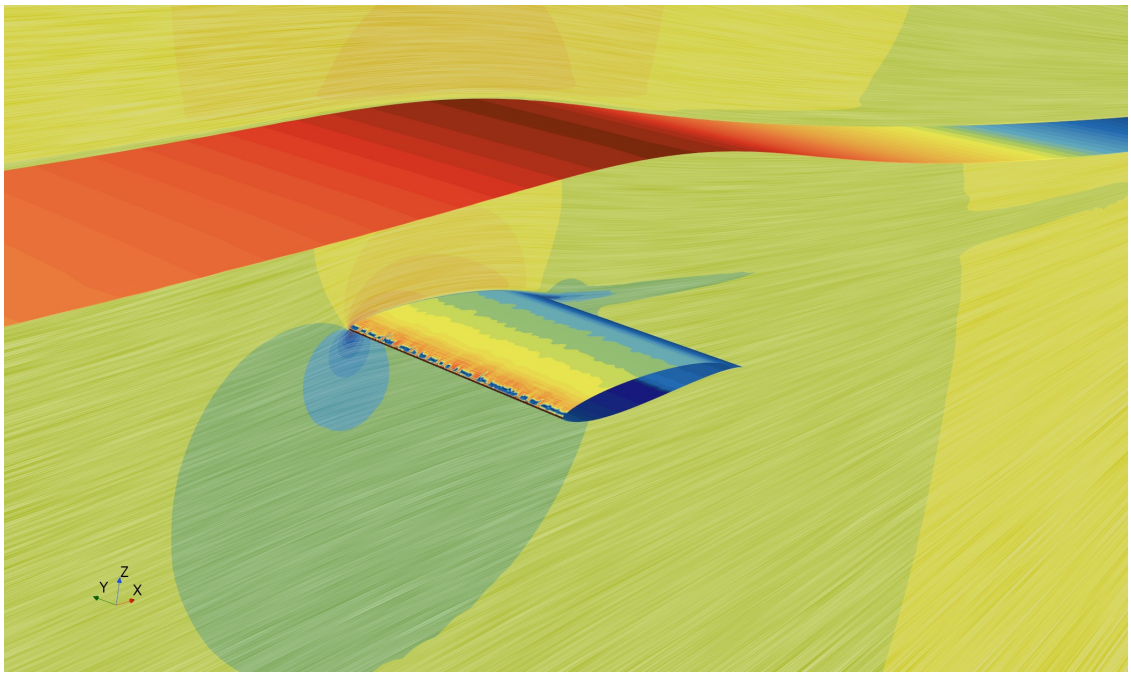

Scaling Effects for Hydrofoil Testing

Developing a methodology for hydrofoil performance measurements in towing tank

Master's thesis in Naval Architecture & Aerospace Engineering

Marcus Varvne, Wilhelm Eriksson

DEPARTMENT OF Mechanics and Maritime Sciences

CHALMERS UNIVERSITY OF TECHNOLOGY
Gothenburg, Sweden 2024
www.chalmers.se

Scaling Effects for Hydrofoil Testing

Developing a methodology for hydrofoil performance measurement in towing tank

Marcus Varvne, Wilhelm Eriksson

CHALMERS
UNIVERSITY OF TECHNOLOGY

Department of Mechanics and Maritime Sciences
Fluid mechanics
Chalmers University of Technology
Gothenburg, Sweden 2024

Scaling Effects for Hydrofoil Testing
Developing a methodology for hydrofoil performance measurement in towing tank
Marcus Varvne, Wilhelm Eriksson

Supervisor: Alex Shiri, RISE Maritime Department
Examiner: Arash Eslamdoost, Mechanics and Maritime Sciences

Master Thesis 2024
Department of Mechanics and Maritime Sciences
Chalmers University of Technology
SE-412 96 Gothenburg
Telephone +46 31 772 1000

Typeset in LaTeX
Printed by Chalmers Reproservice
Gothenburg, Sweden 2024

Abstract

The fast development and growing interest in hydrofoils within marine applications have led to an increased demand for testing and verification of foil designs. Testing model scale hydrofoils is not as straightforward as for traditional displacement hull models. Currently, there does not exist a proposed way of scaling down a hydrofoil. This work sheds light on the issues of different scaling effects and proposes a method to perform model scale testing of a hydrofoil.

This report is an outcome of a master's thesis project within Naval Architecture and Aerospace Engineering at Chalmers University of Technology. The project aims to evaluate different scaling effects on a horizontal hydrofoil and develop a feasible methodology to test foil performance in a towing tank. Limiting factors of the towing tank are identified and flow effects relative to submergence depth and testing velocity are investigated in the Computational Fluid Dynamics software *STAR CCM+*. The results build on a verified solver setup by conducting a turbulence model study. The effects of varying submergence depth and velocity is investigated using a generic profile *Eppler 818*. The characteristics of a wave is shown to have a significant effect on lift.

Keywords: Hydrofoil, scaling, experimental testing, towing tank, free-surface, CFD

Sammanfattning

Den snabba utvecklingen och det växande intresset för bärplan inom den marina sektorn har lett till en ökad efterfrågan för testning och verifiering. Att testa i modellskala är inte lika enkelt som för traditionella fartyg. Det finns idag inget konkret tillvägagångssätt att skala ner ett bärplan för testing. Det här arbetet tar upp problematiken med olika skalningseffekter och föreslår en metod för att kunna testa bärplan.

Rapporten är ett resultat av ett examensarbete inom Naval Architecture and Aerospace Engineering vid Chalmers tekniska högskola. Projektet syftar utvärdera olika skalningseffekter på en horisontell vinge under vatten och utveckla en lämplig metod för att testa bärplan i en släpanläggning. Faktorer så som testdjup och hastighet undersöks med numeriska beräkningar i *STAR CCM+*. Resultaten bygger på en verifierad beräkningsmodell genom att genomföra en turbulensmodellstudie. Vidare undersöks hur olika nedsänkningsdjup och hastigheter påverkar resultaten genome att köra simuleringar för en generisk profil *Eppler 818*. Det visar sig att lyftkraften är starkt beroende på om flödet har ett Froudtal större eller mindre än ett.

Nyckelord: Bärplan, skalning, testning, släpanläggning, CFD

Acknowledgements

We would like to express our sincere gratitude to our Chalmers supervisor Arash Eslamdoost and to our RISE supervisor Alex Shiri, for their ongoing support and invaluable contributions throughout the project. Their expertise in project execution and their knowledge in their respective field of research have consistently proven invaluable.

Our gratitude also extends to the following:

- Magnus Wikander from *RISE*, who gave feedback throughout the project and guidance in customers needs.
- Adam Persson from *RISE* who supported in the choice of a modern foil proile.
- Da-Qing Li from *RISE* who supported CFD simulation setup.
- Gabriele Mazza from *RISE* who supported in the CFD Simulations and discussions.

Wilhelm Eriksson
Marcus Varvne

List of Acronyms

Below is the list of acronyms that have been used throughout this thesis listed in alphabetical order:

AMR	Adaptive Mesh Refinement
AOA	Angle of Attack
AR	Aspect Ratio
CAD	Computer Aided Design
CFD	Computational Fluid Dynamics
CFL	Courant–Friedrichs–Lewy
CFRP	Carbon Fiber Reinforced Polymer
DES	Detached Eddy Dimulation
EFD	Experimental Fluid Dynamics
ITTC	International Towing Tank Conference
LES	Large Eddy Simulation
NACA	National Advisory Committee for Aeronautics
SGS	Subgrid-Scale
SSPA	SSPA Sweden AB
SST	Shear Stress Transport
RANS	Raynolds Avereged Navier-Stokes
RE	Reynolds number
RISE	Research Institutes of Sweden AB
VOF	Volume of Fluid

Nomenclature

Below is the nomenclature of indices, sets, parameters, and variables that have been used throughout this thesis.

γ	Penalty coefficient
Δt	Time discretization step (time interval)
V	Velocity [m/s]
L	Lift [N]
C_L	Lift coefficient
D	Drag [N]
C_D	Drag coefficient
C_{D0}	Pressure drag coefficient
C_{Df}	Skin friction drag coefficient
C_{Din}	Induced drag coefficient
C_{Di}	Interference drag coefficient
ρ	Density $[kg/m^3]$
A_p	Projected area $[m^2]$
P_s	Surface pressure $[Pa]$
P_v	Vapor pressure $[Pa]$
P_∞	Static pressure $[Pa]$
P_{atm}	Atmospheric pressure $[Pa]$
∇p	Pressure gradient
Fn_c	Chord base Froude number
Fn_h	Height base Froude number
g	Gravity $[m/s^2]$
c	Chord length $[m]$
ν	Dynamic viscosity $[PaS]$
σ	Cavitation number
k	Kinetic energy $[J]$

ϵ	Dissipation rate $[m^2/s^3]$
Δx	Mesh size of first cell $[m]$

Contents

List of Figures

List of Tables

1

Introduction

When flow physics from aircraft meets marine vessels, a conflict arises regarding scaling. When scaling for wave drag of a displacement vessel, the size of the model is decreased and the speed is lowered. Conversely, for a wing, the opposite is true, and either the size needs to be increased or the speed adjusted accordingly. This discrepancy in scaling requirements creates a challenge when trying to compare flow physics.

In the traditional case of marine vessels, particularly displacement vessels, the dominant forces at play are typically related to wave drag and hull resistance. As the size of the model is decreased, the Froude number (a dimensionless number representing the ratio of inertia to gravity forces in a flow) decreases as well. To maintain similarity between the model and the full-scale vessel, the speed is usually lowered since wave drag is directly related to the Froude number. On the other hand, for aircraft wings, the dominant forces are typically related to lift and aerodynamic drag. As the size of the model decreases, the Reynolds number (a dimensionless number representing the ratio of inertial forces to viscous forces in a flow) decreases. To maintain similarity between the model and the full-scale aircraft, the size of the model needs to be increased or the speed increased because aerodynamic forces are directly related to the Reynolds number. This difference in scaling requirements leads to conflicts when attempting to conduct experiments or simulations on hydrofoiling vessels.

This work is part of a larger project at *RISE Research Institutes of Sweden* and *Chalmers*, financed by *Trafikverket* through *Lighthouse*. The project aims to develop a test rig at *SSPA Maritime Center* to carry out hydrofoil test in presence of water free-surface.

1.1 Background

The rapid development and commercialization of foiling inter-city ferries, day cruisers, sailing boats, and other marine vessels have led to an increased number of interested parties and a demand for testing different foil designs as part of the development of new platforms. With hydrofoils lifting the vessel out of the water, understanding the hydrodynamics of a fully submerged wing is essential. Typical operating speeds for modern foil applications are in the range of 20-35 *knots*.

Several studies have concluded that operating a lifting device close to the free surface corresponds to a lower lift. It is critical to understand the physics that governs this behavior in order to come up with robust, efficient, designs and testing methods.

Testing is a vital step to verify the design before it reaches production. With the large commercialization and public operation, safety, as well as performance optimizations, are crucial to mitigate risks and ensure successful development of the foiling spectrum within marine operations. Traditionally, testing of displacement marine vessels is conducted by experimental testing in towing tanks and wave labs to determine resistance, maneuvering,

and seakeeping capabilities. Hydrodynamic model tests are of importance to verify design concepts, verification of numerical models and to help understand physical problems [15].

1.2 Objective

The objectives of this project are to evaluate different scaling effects on a horizontal hydrofoil and then propose guidelines for identifying the feasibility of the test in *SSPA's* towing tank (including hydrofoil dimensions and test speed).

1.3 Limitations

The limitations of the project are categorized into three aspects that significantly influence the quality of the work. The different aspects are budget, scope, and time. The interplay between these factors determines the quality of work.

The project was awarded a grant of 100,000 *SEK* from the *Rolf Sörmans Foundation*, for the construction of a hydrofoil and test in the towing tank at *SSPA*. The application was sent at the beginning of the project. However, due to the timing of the grant approval, which occurred halfway through the project duration, the project was constructed to work without funding.

With a time-frame of 5 *months* for this work, computational simulations emerged as the main focus for collecting data, while physical tests were not feasible to conduct within the time-frame after approved funding.

The scope of the project aimed to investigate the possibilities of creating a methodology to test hydrofoils in the towing tank at *SSPA* with its current limitations. Consequently, reliance on computational simulation was deemed sufficient for identifying correlations and patterns to draw meaningful conclusions. Although validating the results through towing tank tests is essential, it is not included in this work due to time limitations.

2

Theory

A vast amount of research has been conducted on flow theory, both in and out of water. The aerospace industry has contributed with extended knowledge about the flow around airfoils which has led to the development of new optimized profiles. At the same time, the marine industry has explored flow dynamics in water, focusing on hull design and propulsion systems. The research includes large numbers of both numerical and experimental studies, in air and water.

2.1 Hydrofoil geometry

With the conducted research, aerodynamically tailored and mission-optimized profiles have been developed since way back in time. Today, there are databases with plenty of airfoil profiles to choose from. Common profile families include the *National Advisory Committee for Aeronautics (NACA)*, *Eppler* and *Clark Y* airfoils. With the vast amount of profiles available, the data should carefully be reviewed to select a profile that matches the intended use. Commonly, these airfoils are further developed and optimized for the specific application. For this work, the horizontal foil should be lift-generating, and thus an asymmetric, cambered profile was a good start.

2.2 Flow theory

A profound understanding of fluid dynamics around a hydrofoil is fundamental for designing efficient and seaworthy foiling vessels. Comprehending how various aspects of fluid flow affect performance is crucial for assessing and improving vessel efficiency and seaworthiness.

2.2.1 Lift and drag

Within aerodynamics, lift and drag represent two fundamental forces that govern the behavior of a wing that moves through a fluid. Lift is the aerodynamic force generated perpendicular to the flow direction, while drag is the resistance force acting parallel to the flow direction, see Figure 2.1. The forces are influenced by several factors, including the shape and profile of the wing, the angle of attack, and the aspect ratio. Additionally, the non-dimensional lift and drag coefficients, denoted by C_L and C_D respectively, are commonly used to determine the aerodynamic characteristics of a wing.

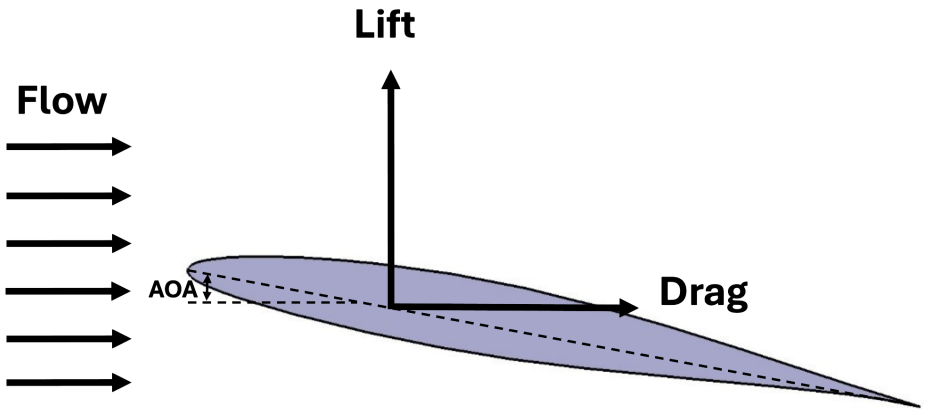

Figure 2.1: Lift and drag from a hydrofoil

The lift force, as expressed by Equation 2.1, is proportional to the square of the fluid velocity (V), the density of the fluid (ρ), the projected area of the wing (A_p), and the lift coefficient. Similarly, the drag force, as depicted in Equation 2.2, is influenced by the same factors but is instead determined by the drag coefficient.

The lift and drag coefficients are usually plotted in a graph as the lift-to-drag ratio (L/D). The L/D, as defined by Equation 2.3, serves as a crucial performance metric in aerodynamic design. Generally, the goal is to minimize drag for a required amount of lift at a certain design speed.

$$L = \frac{1}{2}\rho V^2 A_p C_L \tag{2.1}$$

$$D = \frac{1}{2}\rho V^2 A_p C_D \tag{2.2}$$

$$L/D = \frac{C_L}{C_D}. \tag{2.3}$$

From classic aerodynamics, the drag force acting on a wing can be dissected into various components, each stemming from different sources of drag, as delineated by Equation 2.4:

$$C_D = C_{D0} + C_{Df} + C_{Dind} + C_{Di}. \tag{2.4}$$

Here, C_{D0} represents the pressure drag, which arises from the pressure differential between the upper and lower surfaces of the wing. This component is primarily influenced by the shape and profile of the wing, as well as the angle of attack.

The term C_{Df} denotes the skin friction drag, which results from the viscous effects of the fluid along the surface of the wing. This drag component is dependent on the roughness of the wing surface and the velocity gradient near the surface.

Induced drag, represented by C_{Dind}, arises due to the generation of lift. As the wing produces lift, it also induces a downward airflow, resulting in a rearward component of

the aerodynamic force, which contributes to drag. Induced drag is directly proportional to the lift generated by the wing and inversely proportional to the aspect ratio.

Lastly, interference drag, denoted by C_{Di}, accounts for the drag incurred due to the interaction between various components of the aircraft or between multiple wings. This drag component can arise from factors such as wing-fuselage interaction or wing-wing interaction in multi-wing configurations.

2.2.2 Pressure distribution

For an asymmetrical airfoil, the flow gets accelerated along the upper side, creating a low pressure. This is generally referred to as the suction side, while the lower side is referred to as the pressure side. The pressure difference between the suction side and the pressure side is directly linked to the generated lift and is influenced by a number of factors. The pressure coefficient C_p can be defined as

$$\frac{P_s - P_\infty}{\frac{1}{2}\rho_0 U_\infty^2} = C_p = 1 - (\frac{U_s}{U_\infty})^2 \tag{2.5}$$

where P_s is the surface pressure, U_s the surface velocity, $P\infty$, static pressure upstream, U_∞ the free stream velocity, and ρ_0 the density of the fluid. As the hydrostatic pressure changes with depth, the ambient pressure will change for different submergence depths which will affect the surface pressure of the foil by

$$P_h = P_{atm}\rho g h, \tag{2.6}$$

where $P_{atm}$is the atmospheric pressure, g acceleration due to gravity, and h is the depth measured from the surface to the leading edge of the hydrofoil.

2.2.3 Boundary layer development

The transition from laminar to turbulent flow is hard to predict and depends not only on Raynolds number, but on other factors such as the profile of the foil, surface finish, and other external triggers. In laminar flow, the boundary layer velocity profile is slimmer compared to turbulent flow which results in less frictional resistance. However, due to lower momentum of the boundary layer it is more prone to flow separation. Turbulent flow, with its higher kinetic energy in the boundary layer, helps to keep the flow attached longer. A wing with turbulent flow can generally operate at a greater angle of attack without experiencing flow separation, a phenomenon that would otherwise significantly diminish lift and elevate pressure drag. Nonetheless, this advantage is counterbalanced by heightened skin friction drag attributable to the thicker boundary layer associated with turbulent flow. Conversely, the operation within the laminar region is characterized by unpredictability, as laminar flow is prone to separation under varying conditions, necessitating controlled environments for reliable performance. Predicting the transition point can be challenging due to its sensitivity to various factors. To address this issue, the boundary layer can be artificially tripped at the leading edge to deliberately determine the location of the transition point. This technique is frequently employed in research and is currently advocated by *ITTC.*[1]. Flow separation is a crucial phenomenon that can have a great impact on the functionality of a wing. It occurs when the fluid boundary layer separates from the surface, disrupting the flow and resulting in reduced lift. The transition from laminar to turbulent flow, as discussed earlier, plays a significant role in determining the likelihood of flow separation.

2.3 Scaling effects

The aim of conducting physical model scale testing is to replicate the behavior of the full-scale design as accurately as possible while minimizing resource requirements. The behavior of a model is governed by certain modeling laws, which are derived by comparing the ratios of various forces within the system. Achieving similarity in forces requires satisfying geometrical, kinematic, and dynamic similarity criteria.

When a model and a full-scale prototype are geometrically similar, they are scaled with a constant ratio between all dimensions. This applies not only to the dimensions of the structure itself but also to the surrounding environment. For instance, in the case of an marine vessel, the depth between the vessel and the seabed must be scaled proportionally to achieve geometric similarity. Additionally, the motion of the structure must be scaled so that the ratio between all motions matches that of the full-scale structure. Dynamic similarity is achieved when all forces are scaled in both magnitude and direction. For hydrofoils and marine vessels, three dimensionless quantities are particularly relevant:

- Froude Number
- Reynolds Number
- Cavitation Number

2.3.1 Froude number

The Froude number is the ratio between inertia forces and gravitational force and can be expressed in relation to characteristic length or depth. The relations can be calculated as:

$$Fn_c = \frac{V}{\sqrt{g \cdot c}} \tag{2.7}$$

$$Fn_h = \frac{V}{\sqrt{g \cdot h}}, \tag{2.8}$$

where V is the vessel's speed, g is the gravitational acceleration, c is the chord length and h is submergence-depth, respectively, when calculating for a hydrofoil. If geometrical and kinematic similarities occur with matching Froude numbers, wave resistance will scale correctly since surface waves occur due to gravitational forces.

2.3.2 Reynolds number

Reynolds number represents the ratio between inertia and viscous forces. If Reynolds number similarity occurs between model and full-scale structure, then correct viscous forces can be assumed. Reynolds number is defined as:

$$R_e = \frac{V \cdot c}{\upsilon}, \tag{2.9}$$

where R_e is the Reynolds number and υ is the kinematic viscosity. For a fully submerged hydrofoil that has water flow across the surface at all times, the viscous forces will be of importance which entails that Reynolds number similarity is of importance.

Achieving Reynolds similarities will, most likely, result in high speed if the hydrofoil is scaled down. Although matching the Reynolds number completely can be difficult it is of more importance to match the flow regime, i.e. laminar or turbulent, for full scale and model scale. Commonly, a similar flow behavior is seen for a range of Reynolds numbers [7]. If Reynolds similarities is not possible, a solution could be to trip the flow, which gives control of the transition from laminar to turbulent flow.

2.3.3 Cavitation number

Cavitation occurs when the local pressure around the foil reaches the vapor pressure of the fluid. The cavitation number shows the relation between these two pressures and is defined as

$$\sigma = \frac{p - p_v}{\frac{1}{2} \cdot \rho \cdot V^2}, \tag{2.10}$$

where ρ is the density, p is the local pressure, p_v is the vapor pressure and V is the velocity of the flow. When the cavitation number is high (i.e., significantly greater than 1), it indicates that the local pressure is much higher than the vapor pressure, and cavitation is unlikely to occur. Conversely, when the cavitation number is low (i.e., close to or less than 1), it suggests that the local pressure is approaching or falling below the vapor pressure, increasing the likelihood of cavitation. This can lead to the formation of vapor bubbles that collapse violently, potentially causing significant damage to the foil's surface and reducing its overall performance. Additionally, it can result in increased noise and vibration.

2.4 Towing tank

A towing tank is, in its simplicity, a long and confined basin filled with water. More precisely, a facility to investigate the hydrodynamics of a model in a controlled environment. The model is connected to a towing carriage, which can move along the length of the tank at different speeds. The tank at SSPA is equipped with flap-type wave generators that can generate both regular and irregular waves along the basin to replicate different sea conditions. The carriage acts as a working platform that carries measuring equipment and can be modified to fit different instrumentation such as force sensors, pressure transducers, or cameras, both under and above the water. The tank is primarily used for hull and propeller form optimization but can facilitate a variety of vessels due to its modularity.

Data, including dimensions for the towing tank at *SSPA*, can be found in Table 2.1.

Table 2.1: Main particulars of *SSPA's* towing tank

Length	Breadth	Water depth	Max speed	Acceleration
260 m	10 m	5 m	10 m/s	1 m/s^2

From the values in Table 2.1, the measurement time at constant maximum speed is calculated as follows:

$$t_{acc} = \frac{v - u}{a} = \frac{10m/s - 0m/s}{1m/s^2} = 10s \tag{2.11}$$

$$d_{acc} = \frac{1}{2} \cdot a \cdot t_{acc}^2 = \frac{1}{2} \cdot 1m/s^2 \cdot 10s^2 = 50m \tag{2.12}$$

$$t_{measuring} = \frac{(d_{tank} - 2 \cdot d_{acc})}{v} = \frac{160m}{10m/s} = 16s, \tag{2.13}$$

here we assume that the rig can decelerate with the same magnitude as it accelerates. Thus, the braking distance and starting distance, d_{acc} are the same, and d_{tank} is the total operational length of the towing tank. Operating the carriage at maximum speed, the total measuring time $t_{measuring}$ becomes 16 *seconds*.

2.4.1 Restrictions in available testing method

Although hydrofoils have been around for a long time, a clear procedure for testing is absent. The 29th International Towing Tank Conference[1] addressed the issue of scale effects on foils. The Reynolds number will be different from full scale to model scale and matching Froude and Reynolds number simultaneously is impossible. The conference proposed further investigation into using *Computational Fluid Dynamics*, *CFD*, to adjust the lifting devices for the model scale so that they match the forces at full scale.

Limiting factors in *SSPA's* towing tank are length, acceleration, and maximum speed. These are limitations that have not been a problem when testing traditional displacement vessels. With foils, however, if the size is down-scaled the speed has to be increased and vice versa to ensure similar flow behavior and accurate measurements. The other limiting factor is the considerable vertical lift force generated with the hydrofoil if the Reynolds number scaling is applied to the hydrofoil.

2.4.2 Free surface effects

It is clear from previous studies that operating a horizontal hydrofoil in close proximity to the surface has several effects on its performance. Studies have been conducted on various phenomena such as cavitation, separation, and the effect on lift and drag. Ni *et al.* [8] showed that operating close to the free surface, especially at high angles of attack, could delay stall. The presence of motion-induced free surface waves leads to heightened flow velocities that enhance momentum within the boundary layer on the suction side, thus effectively preventing flow separation. It should be mentioned that Reynolds number was relatively low at 10^5 and extreme effects such as ventilation are not considered in the study. A non-dimensional submergence factor h/c is formulated as a ratio between submergence depth h and chord c, where a value of $4-5$ is commonly considered as deep water which means that the free surface has minimal influence on the performance below this depth. However, these recommendations have been developed for specific profiles at specific operating conditions. A highly loaded foil will most likely affect the free surface differently than a less loaded hydrofoil due to its difference in pressure. To put the individual cases in perspective, a deeper understanding of how the free surface affects the pressure distribution on the arbitrary profile is needed.

To understand the physics better, we start by looking at cars where investigations on ground effects are extensive. Within racing, it is widely known that operating a car at a low ground clearance can help to improve downforce (negative lift) if the undertray is designed properly. This happens as the undertray of the car and the ground acts as a duct that, as a result of the mass conservation law, accelerates the flow. With a higher flow velocity comes a lower pressure and as the pressure difference between the upper and lower sides of the car increases, the negative lift increases as well. This is true up to a point where the ground clearance becomes less or equal to the total boundary layer thickness of the car and the ground, as the flow inside the boundary layer is slower than the freestream.

In theory, if the water surface was assumed to be rigid, the same effect could be expected for a hydrofoil in close proximity to the free surface. However, it is clear that the surface is moving and thus creating waves which brings complexity to the problem. Karim *et al.* [6] showed with numerical *CFD* simulations, in agreement with the venturi effect, that a lower pressure is formed over the suction side at moderate submergence for Fn = 0.5711 and Re = 159,000, corresponding to increased lift. This theory is further strengthened with numerical results from Andersson and Granli[10].

Pernod *et al.* [9] performed another numerical study of a symmetrical profile with a chord-based Froude number of 0.571 and a Reynolds number of 159,000. In close agreement with the theory above, their results showed that lift slightly increases for up to about $h/c = 1$. For lower values, $h/c < 1$, the lift decreases sharply, and for $h/c < 0.5$ the pressure field has changed and the foil produces a negative lift.

2.5 Computational fluid dynamics

The build stones for *CFD* are the conservation laws, which dictate how the flow behaves. The three laws governing the flow physics are:

- **Conservation of mass**, which says that the mass shall remain constant in a closed system over time.
- **Conservation of moment**, Newton's second law states that the acceleration of an object is directly proportional to the net force acting on it and inversely proportional to its mass.
- **Conservation of energy**, which states that energy can not be created or destroyed, only transformed.

Understanding these governing physics is of most importance for accurate simulations and predictions of the flow, as it enables effective modeling of complex fluid flow phenomena with precision and efficiency. This enables researchers and engineers to tackle complex fluid dynamics problems with precision and efficiency.

2.5.1 Navier stokes theorem

The incompressible version of the Navier-Stokes equation describes the motion of a fluid with constant density and delineating the conservation of momentum for fluid flow. It accounts for the interplay between inertial forces, pressure gradients, and viscous forces within a fluid domain. The equation comprises terms representing convection, pressure,

and viscosity effects, to predict the behavior of the fluid.

$$\rho \frac{D\overrightarrow{V}}{D_t} = -\nabla p + \mu \nabla^2 \overrightarrow{V} + \rho g, \tag{2.14}$$

ρ is the density of the fluid, $\frac{D\overrightarrow{V}}{D_t}$ describes the acceleration, $-\nabla p$ is the pressure gradient, $\mu \nabla^2 \overrightarrow{V}$ is the viscosity and ρg is the external forces, in our case, gravity.

2.5.2 Reynolds Avereged Navier-Stokes

Reynolds-Averaged Navier-Stokes (*RANS*) equations form the foundation for simulating turbulent fluid flows by temporally averaging the Navier-Stokes equations. In the *RANS* framework, fluid properties are decomposed into mean and fluctuating components, with the mean variables treated as continuous functions of time. The Reynolds decomposition introduces a Reynolds-averaging operation, yielding time-averaged equations that describe the mean flow behavior. The *RANS* equations account for the momentum transfer, continuity, and energy conservation in a turbulent flow, offering a statistical representation of turbulence effects.

The *RANS* equations for the continuity and momentum conservation, considering an incompressible flow and neglecting body forces, are given by:

$$\frac{\partial \overline{u}_i}{\partial x_i} = 0 \tag{2.15}$$

$$\frac{\partial \overline{u}_i}{\partial t} + \overline{u}_j \frac{\partial \overline{u}_i}{\partial x_j} = -\frac{1}{\rho}\frac{\partial \overline{p}}{\partial x_i} + \nu \frac{\partial^2 \overline{u}_i}{\partial x_j \partial x_j} - \frac{\partial \overline{u_i' u_j'}}{\partial x_j}. \tag{2.16}$$

Here, $\overline{u}_i$ represents the mean velocity components, ρ is the fluid density, ν is the kinematic viscosity, and $\overline{p}$ denotes the mean pressure. The Reynolds stresses $\overline{u_i' u_j'}$ capture the effects of turbulent fluctuations and are crucial for representing turbulence in the averaged equations.

2.5.3 k-Omega SST turbulence model

The k-ω *SST* turbulence model is a combination of the two turbulence models, k-ϵ and k-ω. The model uses k-ϵ in the free stream flow, outside the boundary layer, and uses k-ω closer to the surface, inside the boundary layer. The boundary layer is visualized in Figure 2.2, and is represented by the blue color which is slow speed compared to the free stream speed.

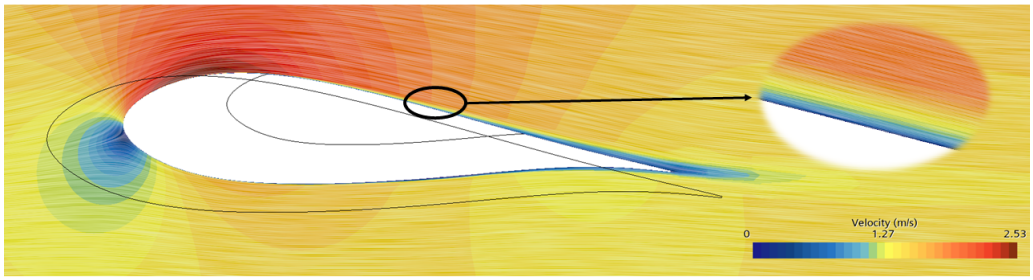

Figure 2.2: Boundary layer development over hydrofoil

Both k-ω and k-ϵ are two-equation models, which means that in addition to the conservation equations, they solve two transport equations. Both models have one common transport equation, which is the turbulent kinetic energy (k), which determines the energy in turbulence[13].

$$\frac{\partial(\rho k)}{\partial t} + \frac{\partial(\rho U_i k)}{\partial x_i} = \frac{\partial}{\partial x_j}\Big[(\mu + \frac{\mu_t}{\sigma_k})\frac{\partial k}{\partial x_j}\Big] + P_k + P_b - \rho\epsilon + S_k, \tag{2.17}$$

where P_k represents the production of turbulent kinetic energy due to mean velocity, and P_b represents the production of turbulence kinetic energy due to buoyancy. σ_k is the Prandtl number for k and S_k is a user defined source.

The other transport equation in k-ϵ is the turbulent dissipation rate(ϵ).

$$\frac{\partial(\rho\epsilon)}{\partial t} + \frac{\partial(\rho U_i \epsilon)}{\partial x_i} = \frac{\partial}{\partial x_j}\Big[(\mu + \frac{\mu_t}{\sigma_\epsilon})\frac{\partial \epsilon}{\partial x_j}\Big] + C_1\frac{\epsilon}{k}(P_k + C_3 P_b) - C_2\rho\frac{\epsilon^2}{k} + S_\epsilon \tag{2.18}$$

C_1,C_2,C_3, and C_μ are coefficients that vary with the change within the turbulence model. S_ϵ and σ_ϵ are the same as in Equation 2.17, but it is instead defined by ϵ and not k.

For k-ω turbulence model the other transport variable is the ω, which represents the specific rate of dissipation of turbulent kinetic energy in the flow. The relationship between ϵ and ω is given by an algebraic relation.

$$\epsilon = C_\mu k\omega \tag{2.19}$$

Through extensive experimental testing, the C_μ coefficient was calculated to be 0.09[12]. With Equation 2.18 and 2.19 can the second transport equation be calculated[13].

$$\frac{\partial(\rho\epsilon}{\partial t} + \frac{\partial(\rho U_i \epsilon)}{\partial x_i} = \frac{\partial}{\partial x_j}\Big[(\mu + \frac{\mu_t}{\sigma_\epsilon})\frac{\partial \epsilon}{\partial x_j}\Big] + \frac{\gamma}{\nu_t}P_k - \beta\rho\omega^2 \tag{2.20}$$

Combining the two models contributes to a robust and computational cheep simulation in the free stream flow with the use of the k-ϵ model and when analyzing the more complex flow close to a surface, k-ω model is used, due to its superior performance for wall-bounded boundary layer, free shear, and low Reynolds number flows[11].

In this turbulence model, three different transition models are used. For many systems, the transition is of no importance and therefore not simulated, but for a hydrofoil, the transition will have a significant impact on the lift and drag. One example where transition models are necessary is when a separation bubble is present, which cannot be captured with the use of only a turbulence model. The first and most simple transition model is the *Gamma transition*, this is a one-equation model and it only solves the turbulence intermittency, and the transport equation for for moment thickness is not accounted for. The second model is the *Gamma-ReTheta transition* model, this model adds the neglected transport equation in the *Gamma transition* model. The third model is the turbulence suppression model, this model is often used when comparing experimental data to *CFD*

due to knowledge acquired from the experiment, such as the transition point, which is the user input. This makes this model a zero-equation model[4].

2.5.4 Spalart-Allmaras Turbulence Model

Spalart-Allmaras turbulence model is a one-equation model, which solves a single transport equation for the eddy viscosity variable, denoted $\tilde{\nu}$. *Spalart-Allmaras* provides a simplified representation of the turbulent flow field compared to more complex models such as *RANS* and *Large Eddy Simulation*(*LES*), which makes it less computationally heavy but still provides accurate results for most flow cases. The transport equation represents the total viscosity of the flow and accounts for diffusion, production, and destruction of the mean flow.

2.5.5 LES turbulence model

LES is a *CFD* approach used to simulate turbulent flow. Unlike the *RANS* model, *LES* resolves a wide range of turbulent scales while modeling the smallest ones.

In *LES*, the flow field is decomposed into resolved large-scale turbulent structures and unresolved small-scale turbulent structures. The large-scale structures are directly simulated, while the small-scale structures are modeled using a subgrid-scale (SGS) model. This allows *LES* to capture the dynamic interactions between the resolved and subgrid-scale turbulence, providing more accurate predictions of complex turbulent flows.

The fundamental principle behind *LES* is to filter out the small-scale turbulence, which is responsible for most of the energy dissipation while retaining the larger-scale structures that contribute significantly to the flow dynamics. This is a more computationally costly model, making *LES* suitable for simulating more detailed turbulent flows.

2.5.6 Detached Eddy Simulation

Detached Eddy Simulation (*DES*) is a hybrid turbulence modeling approach that combines elements of both *RANS* and *LES* methods. *DES* is designed to accurately predict turbulent flow phenomena in regions where both attached and detached boundary layers exist.

In *DES*, the flow field is divided into two regions: a near-wall region where *RANS* modeling is used to resolve the attached boundary layer, and an outer region where *LES* is employed to capture the larger-scale turbulent structures. This allows *DES* to accurately simulate flow separation and reattachment phenomena, which are challenging for traditional *RANS* models.

The transition between *RANS* and *LES* regions in *DES* is governed by a blending function, which switches between the two modeling approaches based on the local flow conditions. In regions of attached boundary layer flow, *RANS* turbulence models are used to resolve the turbulence. In regions of separated flow or complex turbulent structures, *LES* is employed to capture unsteady and large-scale turbulent motions.

2.5.7 Choice of turbulence model

Using *RANS*, there are a number of different turbulence models to choose from to solve the turbulent kinetic energy. k-ω is a well-known model that is commonly used within *CFD*, but it has the drawback of being inaccurate for flow cases with adverse pressure gradients thus it is not a good option if the flow experiences separation. For such cases, the *Spalart-Allamaras* model is proven to perform better.

2.5.8 Physical models

To capture separation and turbulent flow behavior, an implicit unsteady solver is used within *STAR CCM+* combined with a segregated flow model.

2.5.9 Grid

Creating a computational grid for *CFD* involves dividing the domain into cells, using a finer mesh where the solution is of interest and coarser mesh elsewhere. A solution is calculated for each cell and thus a balance between cell size and solution accuracy is of importance for efficient simulations. The grid should be finer near the wing surface and areas of high flow gradients to capture the intricate flow phenomena accurately. Conversely, coarser grid regions can be employed in areas with less significant flow variation or away from the wing surface to optimize computational efficiency. A base size serves as the reference for subsequent refinements. One common strategy is to perform refinements in percentages of the base size, such as 50%, 25%, 12.5%, and so forth. The built-in growth rate parameter helps to determine the number of cells in transition regions between refinements. To capture viscous effects, the boundary layer needs to be captured within a prism layer mesh.

3

Method

The simulations were carried out using *STAR-CCM+*, a commercial *CFD* software by *Siemens*. First, the numerical set-up was validated and compared to experimental wind tunnel data together with a turbulence model study to ensure accurate modeling and results. Then the *Volume of Fluid* model (VOF) was used to investigate how a free surface affects the flow. This was first done in the same wind tunnel domain, with the same setup as the validation case. Later, a new larger domain was modeled instead. With this domain, Reynolds dependencies as well as a free surface study were conducted. Lastly, an analysis of limiting factors on the *SSPA* towing tank was carried out.

3.1 Validation of turbulence model

Investigating the performance of a hydrofoil with *CFD* is highly dependent on the numerical input and choice of solvers to solve the physics. One important aspect of acquiring accurate results is the choice of turbulence model. The study aims to find the most suitable turbulence model when analyzing the performance of hydrofoils.

3.1.1 Experimental validation case

To investigate if a *CFD* simulation is accurate, it is essential to have an experimental case for comparison. *Delft University of Technology* has performed a wind tunnel test for a non-symmetric airfoil [3]. Three different Reynolds numbers were tested: 1, 2, and 3 *million*. The experiment was tested in air, but in the simulation, the medium was selected to be water. This was done to minimize the change in the simulation when later introducing a free surface.

The experimental setup is described in a paper presented by *De Tavernier, D.A.M.*[3]. The changes made in the simulations were the length of the test section. In the experimental case, the total length of the test section was 2.6 *meters*, and the chord length (c) of the hydrofoil was 0.6 *meters*. Using this domain, the solutions had problem to converge. To avoid this, the total length of the domain was set to 9c, which correlates to 5.4 *meters*. The leading edge of the hydrofoil was positioned 3c from the inlet and 6c from the outlet.

3.1.2 Simulation setup

Computational Domain

The study was conducted on a DU17VAWT197 profile with a chord length of 0.6 *meters* and a span of 1.25 *meters*. To minimize computational cost, only half of the test section was tested, which resulted in a wing span of 0.625 *meters*. The cross-section of the domain

was created to recreate the wind tunnel, see Figure 3.1 for a visualization and Table 3.1 for values.

Table 3.1: Domain size for validation case

Axis	meters	Chord length
X	5.4	9c
Y	0.625	1.04c
Z	1.8	3c

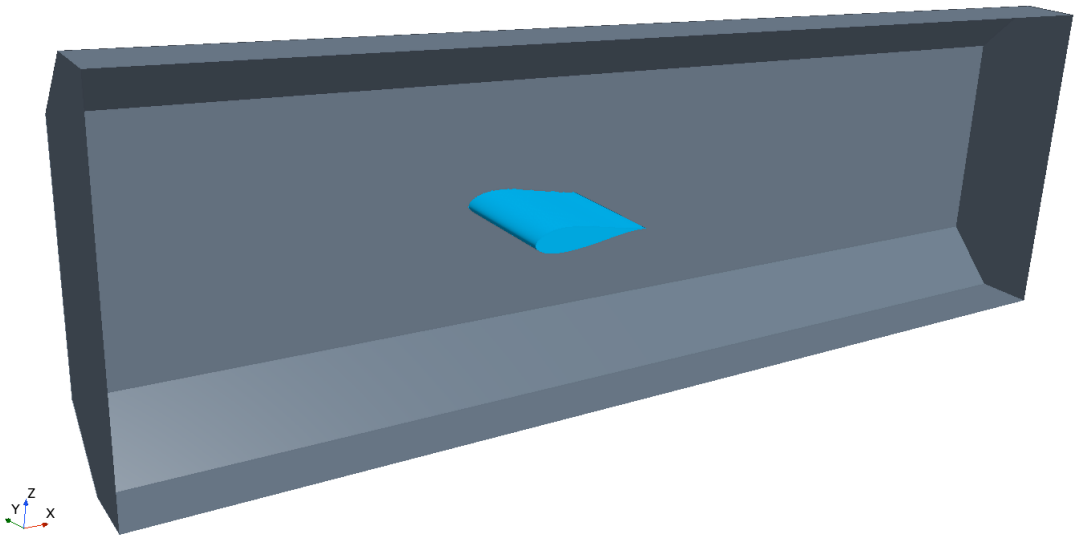

Figure 3.1: 3D view of domain

Mesh

Creating the mesh was a critical step for achieving accurate results, where the precision is directly linked to the mesh's quality. A finer mesh generally leads to more precise outcomes. The mesh conditions were constant throughout all simulations in the project and are listed below:

- Prism layer mesher: This increases the number of cells in the surface normal direction to better capture the boundary layer velocity gradients in this direction. This is necessary to be able to capture boundary layer development close to the wall due to the no slip condition, which entail zero velocity at the wall.
- Surface remesher: This mesh condition refines the surface mesh on the part used in the simulation, a better capture of a part's geometry often implies more accurate results.
- Trimmer: This condition enhances the quality of the mesh and also improves streamline geometry by eliminating unnecessary details and adapting mesh resolution based on local criteria, such as curvature. The trimmer condition optimizes the mesh for accurate flow physics representation while improving computational efficiency. This function smooths sharp edges, simplifies boundaries, and ensures that the mesh aligns well with the geometry.

- Adaptive mesh refinement: *Adaptive mesh refinement* (AMR) improves the mesh by dynamically changing the resolution. The model focus computational resources where they are most needed, based on solution characteristics like gradients or errors. This model creates a more efficient and accurate mesh for complex flow phenomena.

By consistently halving the base dimension, a controlled mesh was achieved. If a random percentage were used, the computer would increase or decrease the mesh in certain locations to be able to create a working mesh, as described in subsection 2.5.9. By utilizing *Volupes* Y+ calculator, the boundary layer total thickness could be approximated to 0.014 *meters* [5]. The number of prism layers was set to 30 with a stretch factor of 1.2 in the wall normal direction, this resulted in a well-captured boundary layer. It was essential for the outermost prism layer to closely match the size of the next cell, this ensured a smooth transition. Moreover, a slow volumetric growth rate was utilized. The general mesh setting can be visualized in Table 3.2. Refinements was done at certain sensitive locations, such as the volume close to the wing, especially at the leading and trailing edge. A refinement was also implemented in the vicinity of an imaginary undisturbed free surface. This was done to minimize the changes when later implementing a free surface. Details of the refinements can be seen in Table 3.2.

Table 3.2: Mesh settings for validation case

Default Controls	
Base Size	0.12
Target Surface Size	25 % relative to base
Minimum Surface Size	0.78125 % relative to base
Surface Curvature	36 pts/circle
Surface Growth Rate	1.1
Number of Prism Layer	11
Prism Layer Stretching	1.2
Prism Layer total Thickness	12.5 % relative to base
Volume Growth Rate	Very Slow
Custom Control on Wing	
Target Surface Size	25 % relative to base
Number of Prism Layer	30
Surface Curvature	360 pts/circle

The free surface refinement was executed in two steps, one large coarse box-shaped refinement, which covers the entire domain in the XY-plane with a thickness of 0.2 *meters*, and one finer that still covers the domain in the XY-plane but with a reduced thickness to 0.05 *meters*, the refinement is symmetric around the free surface. With this setup, the free surface effect can be captured efficiently. The refinement details are presented in Table 3.3.

Table 3.3: Mesh refinement for free surface

Custom control on large surface refinement block	
Trimmed Anisotropic Size Relative to X	12.5 % relative to base
Trimmed Anisotropic Size Relative to Y	25 % relative to base
Trimmed Anisotropic Size Relative to Z	6.25 % relative to base
Custom control on small surface refinement block	
Trimmed Anisotropic Size Relative to X	12.5 % relative to base
Trimmed Anisotropic Size Relative to Y	25 % relative to base
Trimmed Anisotropic Size Relative to Z	1.5625 % relative to base

In addition to the two volumetric refinements introduced on the free surface, four more refinement regions were also introduced. One located on the trailing respectively leading edge, another connecting the free surface and hydrofoil, and finally a wake refinement. The values are presented in the Table 3.4 and coordinates in Table 3.5. Both the leading and trailing edges were configured to be cylindrical with a radius of 0.06 *meters*.

To ensure a uniform mesh setup across all angles of attack, a dynamic volumetric refinement was implemented along the trailing edge. The dynamic refinement was applied by adjusting the position in the z-direction relative to the angle of attack (AOA). Specifically, the position was shifted in the negative z-direction by $tan(AOA) \cdot c$, where c denotes the chord length of the hydrofoil, set to 0.6 *meters* in this study.

Table 3.4: Values for volumetric refinements

Volume	**Trimmer Isotropic size**
Leading edge	1.5625 % relative to base
Trailing edge	1.5625 % relative to base
Between free surface and hydrofoil	12.5 % relative to base
Wake	6.25 % relative to base

Table 3.5: Position of volumetric refinements

	Start Coordinate	**End Coordinate**
Leading edge	[0.0, 2.5, 0.0]	[0.0, 0.0, 0.0]
Trailing edge	[0.6, 0.0, 0.0]	[0.6, 0.625, 0.0]
Between free surface and hydrofoil	[-0.1, 0.0, -0.33]	[1.9, 0.625, -0.112]
Wake	[-0.06, 0.0, -1.0]	[1.8, 0.75, -0.4]

The final mesh contained 12.64 *million* cells. An overview visualization is presented in Figure 3.2 and a close-up on prism layer development and surface mesh of the hydrofoil in Figure 3.3.

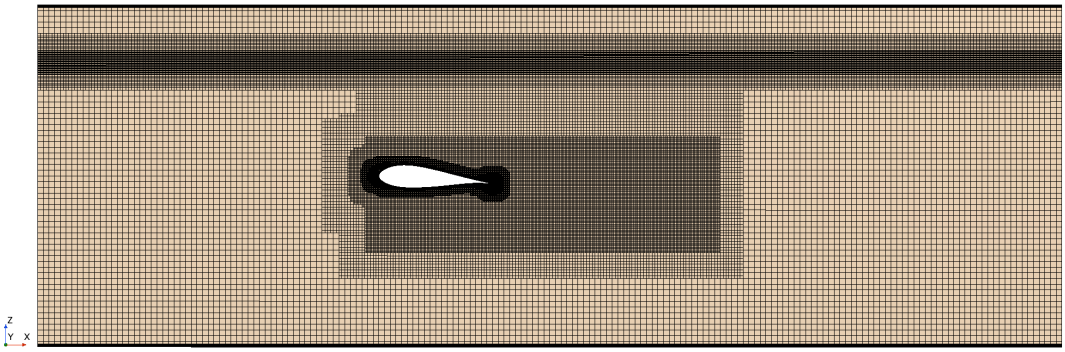

Figure 3.2: Mesh overview

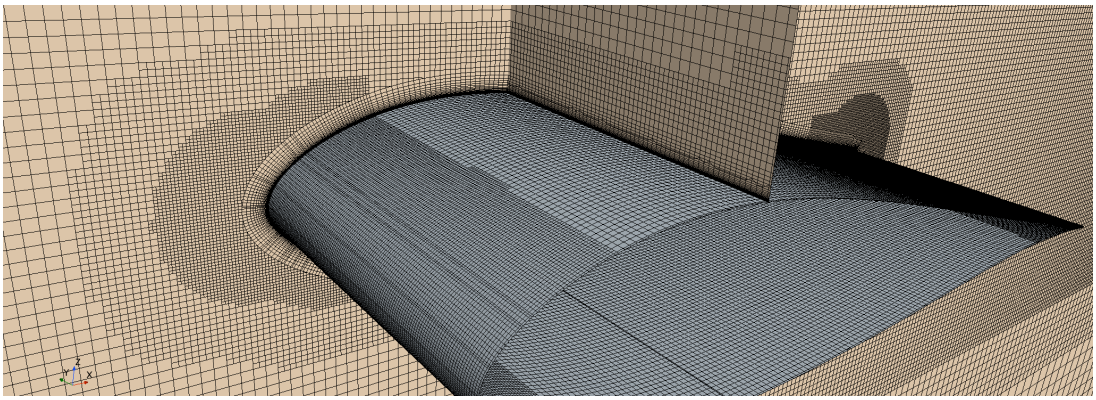

Figure 3.3: Prism layer development and surface mesh on hydrofoil

Time step

The physical models will have a significant impact on the accuracy of the simulation. The implicit unsteady flow was utilized for all simulations, to be able to capture complex unsteady phenomena while maintaining computational efficiency. The time step used for the simulations varies with speed and mesh resolution. The *Courant–Friedrichs–Lewy* (CFL) condition was constant throughout all simulations and was set to 5. The value represents the distance that information travels during the one time step and is dependent on velocity and cell size as described in Equation 3.1,

$$CFL = \frac{U \cdot \Delta t}{\Delta x}, \tag{3.1}$$

where U represents the flow velocity, Δt is the time step, and Δx is the mesh size of the first cell after the prism layer. All parameters are known except for the time step. By consistently using the same mesh, the time step is only dependent on the flow velocity.

A study was conducted to investigate the accuracy of different turbulence models, the result was compared to experimental data to investigate which one coincided the most, see Section 3.1.4.

Boundary conditions

To replicate the flow in the experimental tests, the boundary condition has to be defined correctly. The boundary conditions are listed in Table 3.6. The inlet velocity does not match with the experimental inlet velocity stated by *De Tavernier, D.A.M* [3]. This was due to the change of fluid. In the experiment case air was used which has a lower density than water, which was the fluid used in the simulation. This does not change the drag or lift coefficient as long as the flows operate with the same Reynolds number. With this change, a free surface could later be implemented in the simulation.

To match the flow condition from the wind tunnel, the turbulence intensity at the inlet was set to 0.015 % at the lower speed and to 0.07% at the higher speed, and the turbulent viscosity ratio was set to be 0.0007 [14].

Table 3.6: List of boundary conditions for validation case

Name of boundary	Boundary type	Physical value
Inlet	Velocity inlet	1.48, 2.97, 4.46 [m/s]
Outlet	Pressure outlet	0 [Pa]
Topp	Wall	No slip
Bottom	Wall	No slip
Sym	Symmetry Plane	-
Right	Wall	No slip

3.1.3 Mesh convergence study

A mesh convergence study was conducted to investigate how the results change in relation to the total number of cells. This was done to determine how many cells the simulations needed to acquire accurate results. The setup described in Section 3.1.2 was kept the same with the only parameters varied being related to cell sizes. The turbulence model used in the study was the *k-ω SST*, with *Gamma-ReTheta transition*. The cross-flow parameter is enabled to account for instability in the flow.

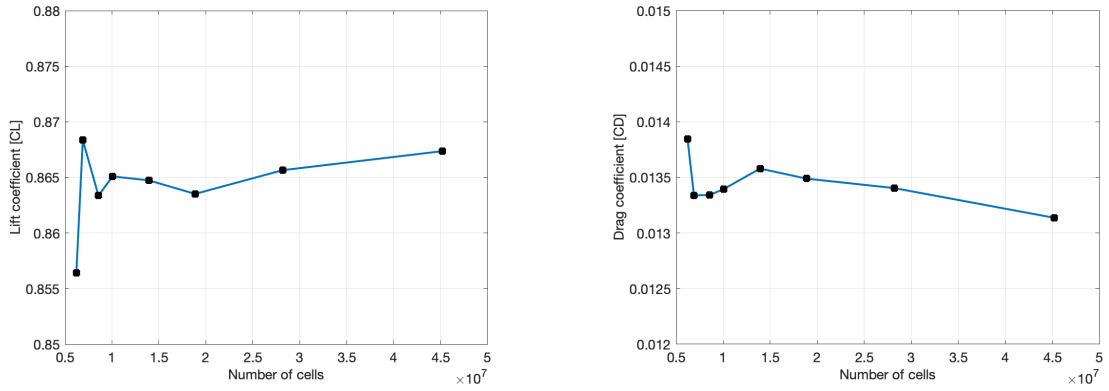

(a) C_L **(b)** C_D

Figure 3.4: Lift and drag coefficients for different computational grid sizes, Re=1 *million*

.

Based on the numerical results presented in Figure 3.4, the lowest C_L of 0.856 is observed at 6.2 *million* cells, while the maximum C_L of 0.868 is achieved at 6.9 *million* cells. The maximum C_D is 0.0138 for 6.2 *million* cells, whereas the minimum C_D is 0.0131 for a cell count of 45.2 *million*. Despite disruptions observed in both lift and drag coefficients at different mesh resolutions, with a 5.3% discrepancy for C_D and a 1.4% discrepancy for C_L, the differences remain relatively small. Therefore, a coarser grid with fewer cells was chosen to conserve computational resources while maintaining an acceptable level of accuracy. The chosen mesh for the rest of the simulations had 12.64 *million* cells.

3.1.4 Turbulence model study

To investigate the accuracy of different turbulence models, a comparison to experimental data at three interesting operation points was done. The points were selected to capture different flow conditions, which resulted in angles of 4, 8, and 12 *degrees*. This selection aimed to capture both normal flow conditions and conditions prone to separation phenomena. Throughout the tests, a consistent Reynolds number of 1 *million* was maintained to ensure uniformity across the tests.

The turbulence models under investigation in this study included the widely-used *Spalart-Allmaras* model, the *k-ω SST* model, and *DES*. Notably, the *k-ω SST* model was evaluated with *Gamma-ReTheta transition* model and without transition model, resulting in a total of four configurations.

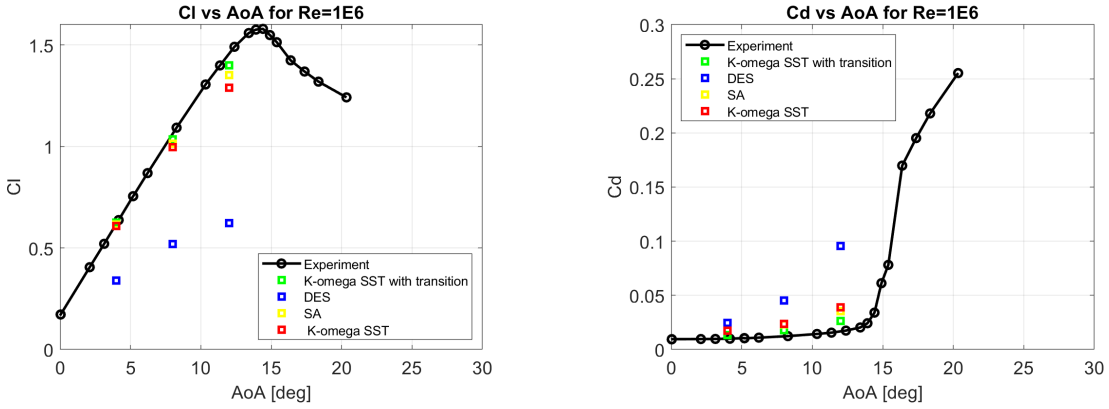

(a) Lift coefficient **(b)** Drag coefficient

Figure 3.5: Lift and drag coefficients for different turbulence models.

At 4 *degrees*, *Spalart-Allmaras* (yellow), *k-ω SST* with transition model (green), and *k-ω SST* without transition model all predicted similar C_L to the experimental data, within 1.78%. At 8 and 12 *degrees*, *k-ω SST* with transition model is the model closest to the experimental data, within 2.54% and 3.97% respectively. *Spalart-Allmaras* predicts a slightly lower lift of $C_L = 1.0134$ for 8 *degrees* and $C_L = 1.35089$ for 12 *degrees*, whereas *k-ω SST* without transition model predicts even lower $C_L = 0.9974$ and $C_L = 1.2891$ respectively. All the data is presented in Table 3.7.

- *k-ω SST* without transition models deviates with 11.48% from the experimental

data at 12 *degrees*, 6.12% at 8 *degrees* and 1.78% at 4 *degrees* for lift. 132% at 12 *degrees*, 94.25% at 8 *degrees* and 74.77% at 4 *degrees* for drag.

- *k-ω SST* with *Gamma-ReTheta transition* model deviates with 3.97% from the experimental data at 12 *degrees*, 2.54% at 8 *degrees* and 1.07% at 4 *degrees* for lift. 58.11% at 12 *degrees*, 48.53% at 8 *degrees* and 33.22% at 4 *degrees* for drag.
- *Spalart-Allmaras* deviates with 7.24% from the experimental data at 12 *degrees*, 4.62% at 8 *degrees* and 0.72% at 4 *degrees* for lift. 111.55% at 12 *degrees*, 90.49% at 8 *degrees* and 74.41% at 4 *degrees* for drag.
- *DES* deviates with 57.29% from the experimental data at 12 *degrees*, 51.06% at 8 *degrees* and 45.21% at 4 *degrees* for lift. 471.92% at 12 *degrees*, 272.85% at 8 *degrees* and 149.34% at 4 *degrees* for drag.

Turbulence model	**4 deg**	**8 deg**	**12 deg**
K-Omega SST, Gamma-ReTheta	1,07%	2,54%	3,97%
K-Omega SST, No transition	1,78%	6,12%	11,48%
Spalart-Allmaras	0,72%	4,62%	7,24%
DES	45,21%	51,06%	57,29%

Table 3.7: Comparison of lift for various turbulence models at different angles of attack

The *DES* predicts a notably lower lift and higher drag for all three cases. The large deviation could be explained by the fact that the model predicted the flow to separate. Figure 3.6 shows the skin friction coefficient together with constrained streamlines on the foil surface and flow velocity around the foil. The constrained streamlines together with the velocity vectors both clearly indicate a separation occurring along the suction side, at about 60% of the chord length, see Figure 3.6a. None of the other models, in accordance with the experimental data, had separation. A comparison of the *k-ω SST* with and without transition model can be seen in Figure 3.6c and 3.6b. Both models showed similar results for lower AOA where no dominant transition effects were present, but as the angle was increased to 12 *degrees*, the *Gamma-ReTheta transition* model captures a different flow state more accurately. The use of *Spalart-Allmaras* shows similar results as *k-ω SST* with no transition, the two turbulence models result in almost identical flow, see Figure 3.6b and 3.6d.

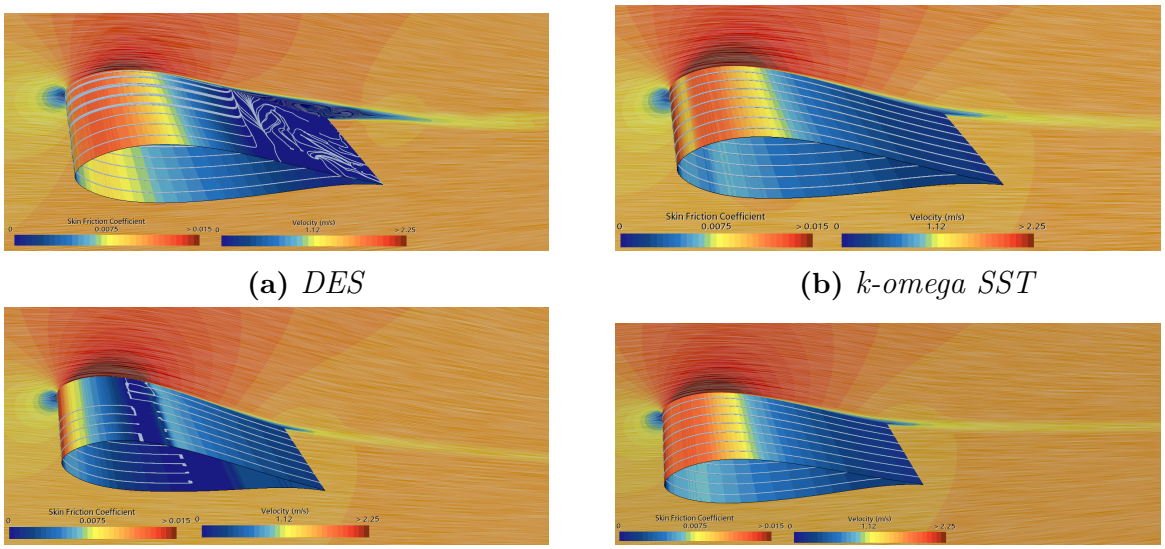

(a) *DES* **(b)** *k-omega SST*

(c) *k-omega SST* with transition **(d)** *Spalart-Allmaras*

Figure 3.6: Velocity vectors with skin friction for different turbulence models

Based on this investigation, a decision was made to move on with the *k-ω SST* with *Gamma-ReTheta transition* model. Further simulations at Re=2 *million* and Re=3 *million* were conducted. Figure 3.7 and Figure 3.8 show the model to match the experimental data for these higher velocities as well.

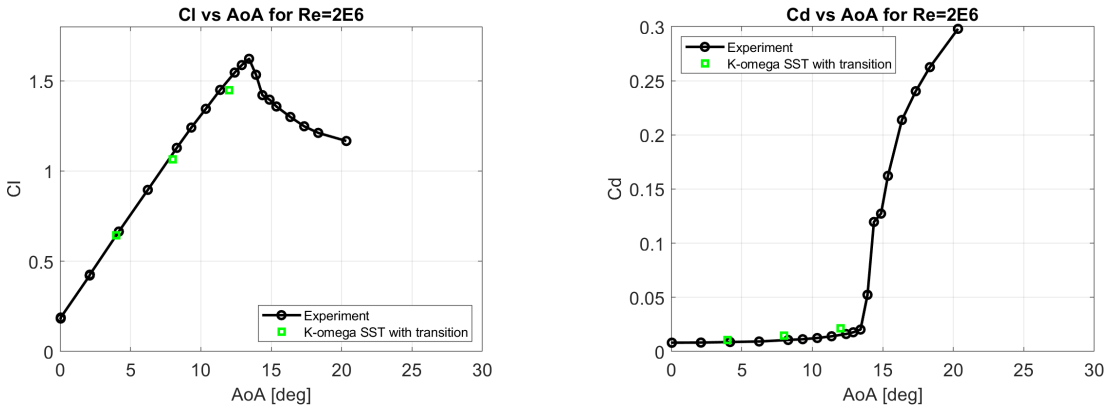

(a) Lift coefficient **(b)** Drag coefficient

Figure 3.7: Lift and drag coefficients for *k-omega SST turbulence* model compared to experimental data at Re=2 *million*.

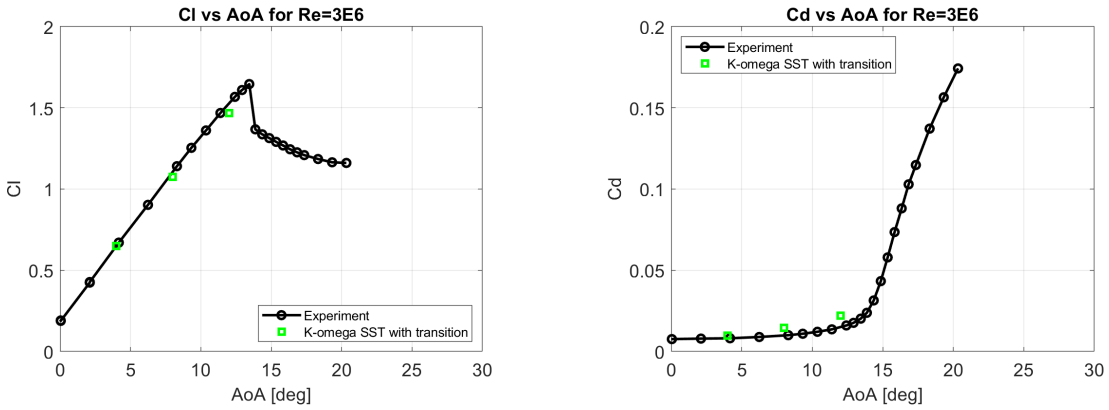

(a) Lift coefficient **(b)** Drag coefficient

Figure 3.8: Lift and drag coefficients for *k-omega SST turbulence* model compared to experimental data at Re=3 *million*.

3.2 Changing computational domain and wing profile

The proposed method was to introduce a free surface in the wind tunnel domain to compare the two cases, with and without a free surface against each other. In practice, it was found that the small wind tunnel domain quickly became limiting with strong wall interactions that caused the simulations to diverge, giving inaccurate results. Figure 3.9 shows a snapshot of the whole domain, flow accelerations can be seen along the domain boundaries, indicating that the domain is too small. Because of this, a larger domain with symmetry planes was created and the more generic *Eppler 818* profile was implemented and tested for different submergence depths and Reynolds dependencies. The new domain setup is further explained in the following sections.

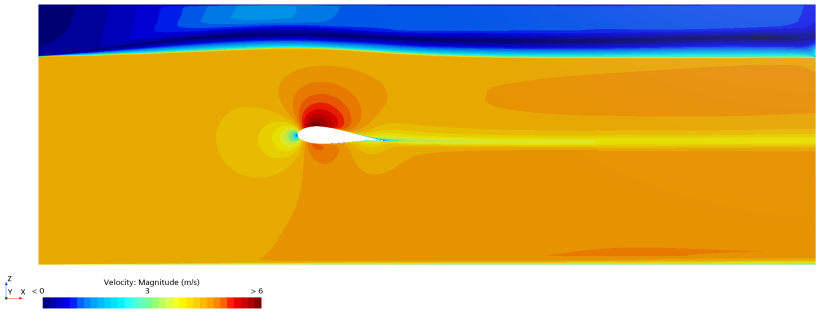

Figure 3.9: Velocity magnitude for wind tunnel with free surface

3.3 Numerical analysis of Reynolds number convergence

A numerical study was conducted to investigate the relationships between lift and drag across a span of Reynolds number in presence of free surface. This study aimed to facilitate testing in towing tanks, where constraints on size and speed often are present.

These limitations influence the Reynolds number, thereby inducing variations in lift and drag characteristics.

3.3.1 Simulation setup

A similar simulation approach was used for this study. The turbulence model was k-ω *SST* with *Gamma-ReTheta transition*, as selected in subsection 3.1.4. The hydrofoil used for this study was the *Eppler 818* with a chord length of 0.6 *meters*, and an operation depth h of 2c, corresponding to 1.2 *meters*. This was set based on a previous study by Pernod et al.[9], who showed that when a hydrofoil is operated two chord lengths below the free surface, the effect on lift and drag will be close to zero, for Reynolds number of 159.000 and AOA of 5 *degrees*.

To investigate the flow behavior around the hydrofoil correctly, a free surface has to be included. The *VOF Wave* model in *STAR CCM+* was therefore implemented. The model includes free surface effects and captures eventual waves generated by the submerged hydrofoil.

Computational domain

The dimensions of the new domain can be seen in Table 3.8. The span of the hydrofoil was set to match the width of the domain, this was done to avoid tip vortex flow. The hydrofoil was centrally positioned along the Y-direction, and in the X-direction, it was situated at one-third distance from the left inlet, equivalent to 10c, see Figure 3.10.

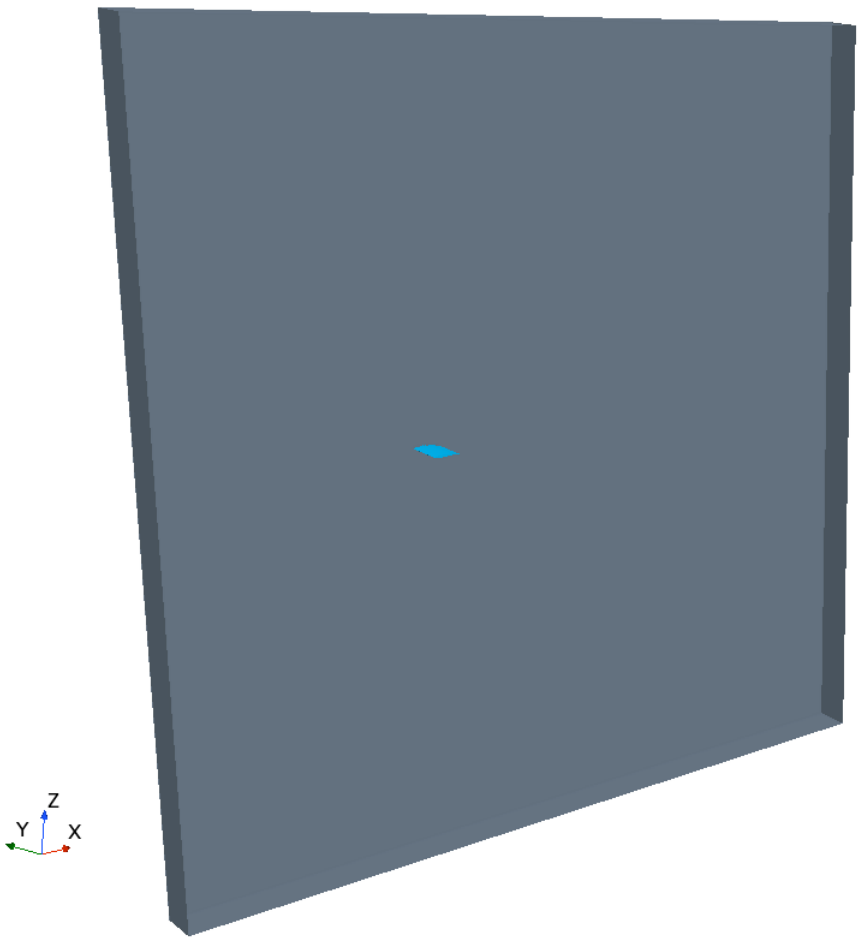

Figure 3.10: 3D view of domain

Table 3.8: New domain size for Reynolds and free surface investigations

Axis	meters	Chord length
X	18	30c
Y	1	1.67c
Z	10	16.67c

Mesh

Due to the extensive number of simulations conducted, the mesh underwent optimization to enhance both accuracy and computational speed. This was achieved by controlling the refinement volumes and minimizing the growth rate. Two main parameters were changed. Firstly, there was an increased volume relative to the size of the hydrofoil. Secondly, the domain has no constrained walls, only an inlet, outlet, and symmetry plane. The default controls and surface control on the wing are visualized in Table 3.9, and a symmetrical cut in the X-Z plane of the mesh is shown in Figure 3.11.

Table 3.9: Mesh settings for validation case

Default Controls	
Base Size	0.2 m
Target Surface Size	400 % relative to base
Minimum Surface Size	0.1953125 % relative to base
Surface Curvature	36 pts/circle
Surface Growth Rate	Fast
Number of Prism Layer	20
Prism Layer Near Wall Thickness	$2 \cdot 10^{-6}$
Prism Layer total Thickness	0.01 m
Volume Growth Rate	Fast
Optimize Cell Topology	On
Custom Control on Wing	
Target Surface Size	6.25 % relative to base
Surface Curvature	360 pts/circle

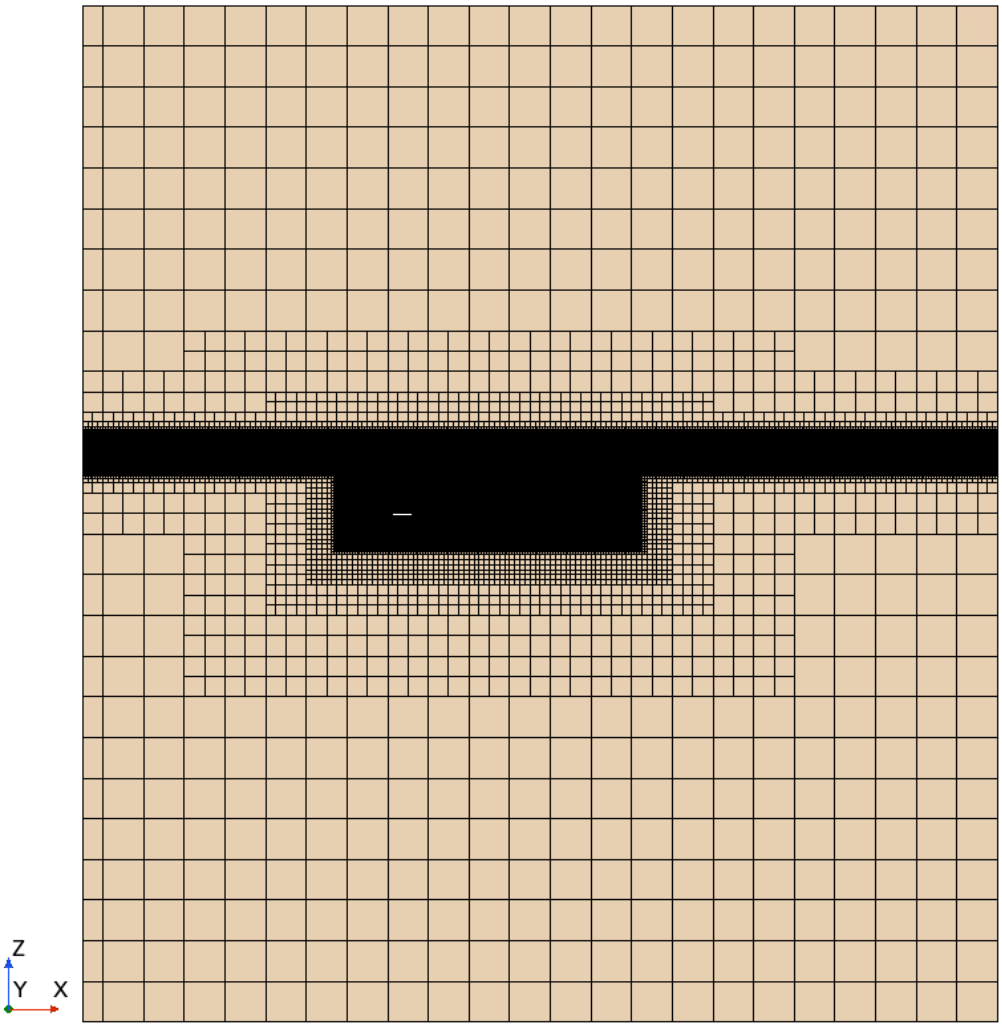

Figure 3.11: Overview mesh

The Free Surface refinement was constructed from two volumes. The first was a large

volume that covered the domain in the X-Y plane and was symmetric around the Z-plane with a total thickness of 0.5 *meters*. The second was a smaller volume that also covered the X-Y plane of the domain and had a thickness of 0.3 *meters*, see Table 3.10 for values and Figure 3.12 for a visualization of the free surface mesh refinement. The goal with the refinements was to keep the wave inside the finer refinements, see Figure 3.13a, and to capture the free surface within 3 cells in the Z-direction, see Figure 3.13b.

Table 3.10: Mesh refinement for free surface

Coarse refinement on free surface	
Trimmed Anisotropic Size Relative to X	25 % relative to base
Trimmed Anisotropic Size Relative to Y	50 % relative to base
Trimmed Anisotropic Size Relative to Z	6.25 % relative to base
Fine refinement on free surface	
Trimmed Anisotropic Size Relative to X	12.5% relative to base
Trimmed Anisotropic Size Relative to Y	50 % relative to base
Trimmed Anisotropic Size Relative to Z	3.125 % relative to base

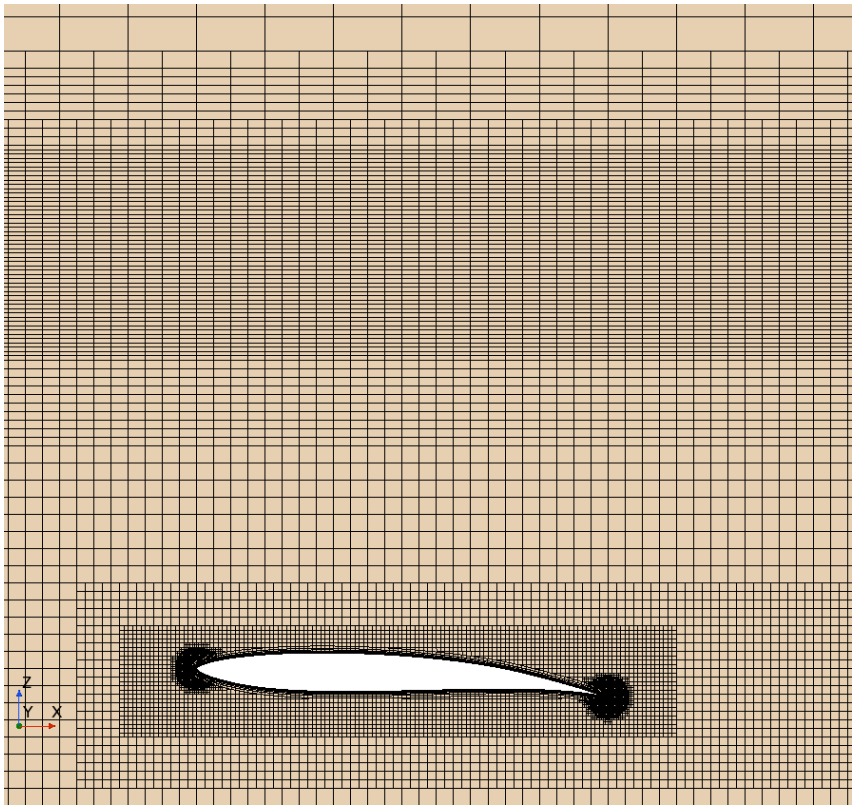

Figure 3.12: Free surface refinement

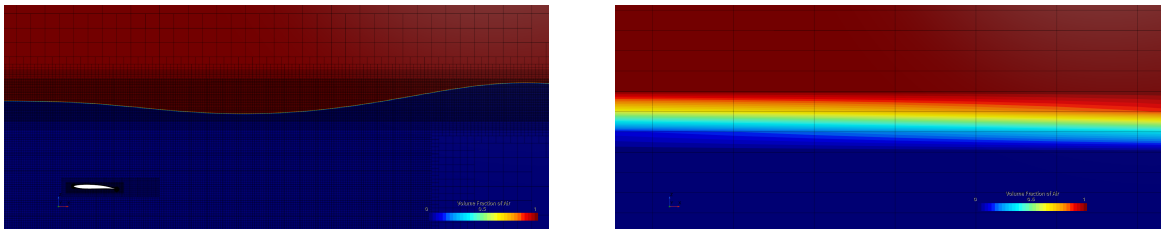

(a) VOF with mesh **(b)** VOF with mesh, free surface

Figure 3.13: Mesh refinement around free surface (a) a general view and (b) a close up view of the interface.

The mesh surrounding the foil underwent refinement using six volumetric refinements, values for each refinement can be observed in Table 3.11 and start and end coordinate in Table 3.12. All refinements were block refinements except for the leading and trailing edge, their cylindrical refinements were used, with a radius of 0.03 *meters*. The mesh was set to change with the submergence of the hydrofoil. All refinements except for the volume refinement that connects the hydrofoil and free surface were transformed with the movement of the hydrofoil, which means maintaining their proximity to the hydrofoil as it moves up and down. The end coordinate for the connection refinement between the hydrofoil and free surface varies with the change of depth and the starting coordinate stays the same. Additionally, the trailing edge coordinate was adjusted to account for variations in the AOA, which was done by having a second transform function on the trailing edge, equal to $\tan(AOA) \cdot c$.

Table 3.11: Volumetric refinements

Volume	**Trimmer Isotropic size**
Leading edge	0.78125 % relative to base
Trailing edge	0.78125 % relative to base
Around hydrofoil	3.125 % relative to base
Between free surface and hydrofoil	12.5 % relative to base
Coarse wake	12.5 % relative to base
Fine wake	6.125 % relative to base

Table 3.12: Volumetric refinements

	Start Coordinate	**End Coordinate**
Leading edge	[0.0, 2.5, 0.0]	[0.0, 0.0, 0.0]
Trailing edge	[0.6, 0.0, 0.0]	[0.6, 2.5, 0.0]
Around hydrofoil	[-0.1, 0.0, 0.05]	[0.7, 1.0, -0.1]
Between free surface and hydrofoil	[-1, 0.0, -Depth-0.7]	[5.0, 1.0, 0.2]
Coarse wake	[-0.2, 0.0, 0.15]	[1.8, 1.0, -0.15]
Fine wake	[-0.15, 0.0, -0.15]	[1.2, 1.0, 0.1]

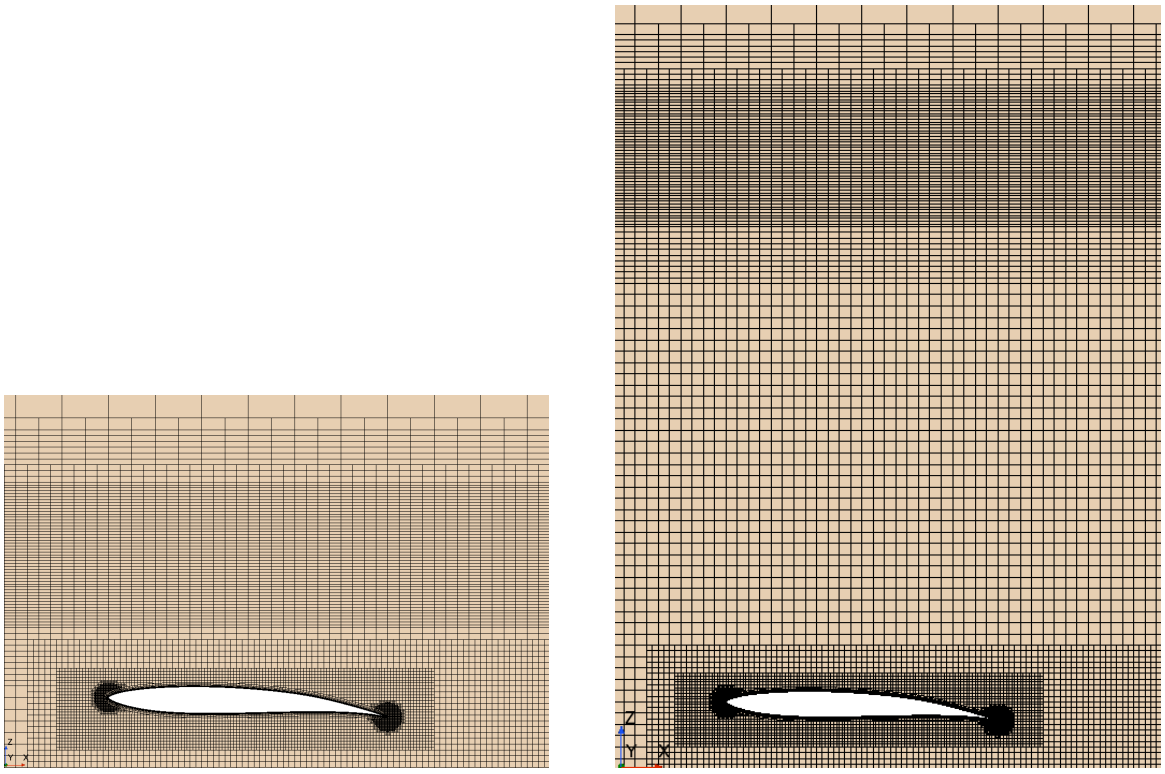

(a) Mesh for 0.5c submergence **(b)** Mesh for 2c submergence

Figure 3.14: Depth dependent mesh

To ensure a seamless transition between the outermost prism layer cell and the next cell, adjustments were made to the prism layer at the leading edge. The thickness was halved to 0.005 *meters* while keeping the number of prism layers, see Figure 3.15. With this adjustment, the y+ could be kept below 1 at the leading edge.

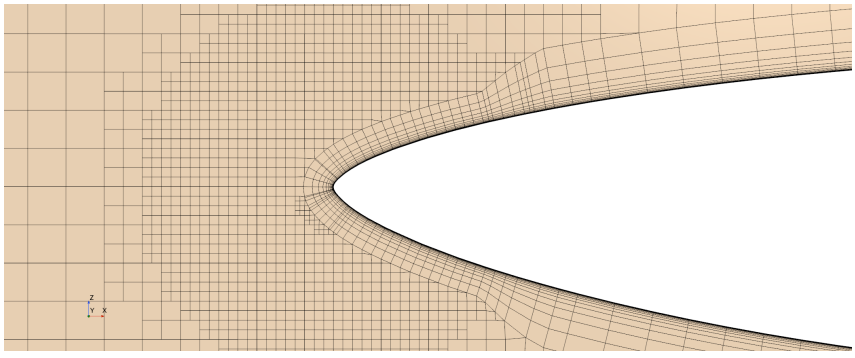

Figure 3.15: Prism layer at the leading edge

The final mesh settings were determined through an iterative process. Refinement sizes were adjusted by analyzing flow characteristics and adding cells where significant flow changes occurred. The focus was directed towards analyzing the scenario where the height base Froude number equaled one, given its distinct wave pattern generation. This was done by ensuring that all waves stayed within the finer free surface refinement. Another parameter iterated to its final value was the number of prism layers, described in subsection 3.3.2. The final mesh resulted in 6040072 cells for 2c submergence.

Region

The boundary conditions used can be seen in Table 3.13. Wave dampening was utilized on the pressure outlet with a wave-damping length of 2.5 *meters*. The backflow specification was set to extrapolated for the pressure outlet. The flow was set to components to only have flow in x-direction, this was done for both air and water flow. The default density values for *STAR-CCM+* were used, corresponding to 997.561 kg/m^3 for water and 1.18415 kg/m^3 for air.

Table 3.13: List of boundary conditions

Name of boundary	Boundary type
Inlet	Velocity inlet
Outlet	Pressure outlet
Top	Symmetry plane
Bottom	Symmetry plane
Symmetry sides	Symmetry plane

Time step

For this study, implicit unsteady was employed for all simulations. A *CFL* number of 3 was utilized consistently throughout all simulations, corresponding to a time-step of 0.0182 *seconds* for an inlet speed of 0.5 *m/s* and 0.000182 *seconds* for an inlet speed of 50 *m/s*. Inner iterations were set to 15.

3.3.2 Mesh convergence study

A mesh convergence study, similar to the one in Section 3.1.3 was performed to ensure good quality mesh. The velocity was set to match the speed of the carriage at 10 *m/s*, corresponding to Re=6.7 *million*. The angle of attack was set to 4 *degrees*. In this investigation, five distinct meshes were evaluated, ranging from 2.5 to 35.4 *million* cells. Consistently, all meshes maintained a uniform thickness for the prism layer to match the boundary layer thickness on the hydrofoil, which was set to 1 *centimeter*. To ensure that the surface was wall resolved, a Y+ was consistently less than 1. This criterion was fulfilled by adjusting the inner layer of the boundary to $2 \cdot 10^{-6}$ *meters* and modifying the number of prism layers to facilitate a seamless transition between the outer boundary layer and the next cell. For this to be possible the stretching factor was set to a free parameter to allow the other to be strict.

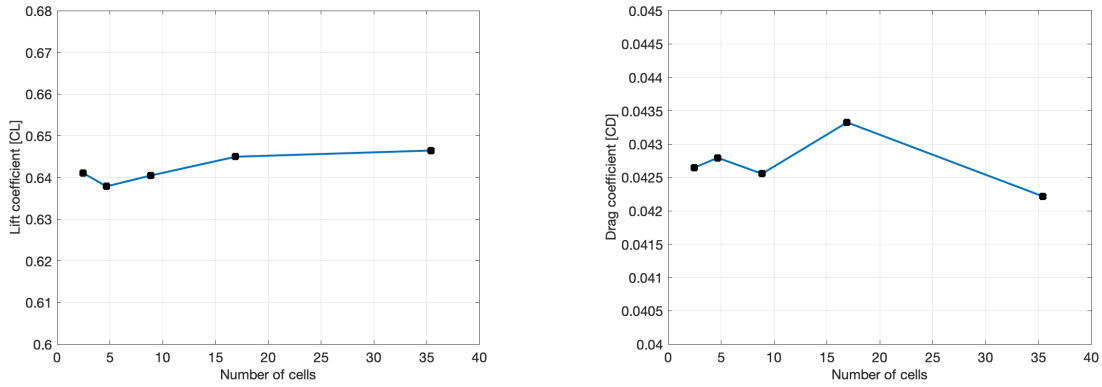

(a) Lift coefficient **(b)** Drag coefficient

Figure 3.16: Lift and drag coefficients for different computational grid sizes.

Figure 3.16 displays varying C_L and C_D with mesh resolutions. The lowest C_L is 0.6379 at 4.68 *million* cells, rising to 0.6465 at 35.4 *million* cells. Maximum C_D is 0.0433 at 16.9 *million* cells, while minimum C_D is 0.0422 at 35.4 *million* cells. Despite minor disruptions, with a 2.6% discrepancy for drag and 1.3% for lift, a coarser grid with fewer cells was chosen to save computational resources.

3.3.3 Cavitation risk analysis

Minimal cavitation is necessary to be able to acquire accurate results for a Reynolds number sweep. If the hydrofoil would cavitate, then it would be necessary to also match the cavitation number, which is not possible when the Reynolds number is matched.

By analyzing the pressure distribution of the hydrofoil and comparing it to the cavitation number, it can be determined whether or not cavitation occurs. If the pressure coefficient exceeds the cavitation number, then cavitation will be present. To reach maximum lift some cavitation is necessary but should be minimized to avoid erosion. Cavitation number is denoted σ and can be calculated as:

$$\sigma = \frac{P - P_v}{0.5 \cdot \rho_{water} \cdot V^2}, \tag{3.2}$$

where P is the pressure and P_v is the vapor pressure of water, which is equal to 2649.6 Pa for 22-*degree* water. V is the flow speed of the fluid and ρ_{water} is equal to 997.56 kg/m^3. The pressure is equal to the atmospheric pressure and hydrostatic pressure.

$$P = P_{atm} + \rho_{water} \cdot g \cdot h, \tag{3.3}$$

where P_{atm} is equal to 101.325 Pa and h is the operation depth. Consistently, $h = 2c$, i.e. 1.2 *meters*.

The pressure coefficient distribution can be seen in Figure 3.17. It can be observed that a cavitation number less than 0.5. induces significant cavitation on the hydrofoil. Using Equation 3.2, the speed corresponds to a cavitation number of 0.5 was 20 m/s. For the

test case, a speed of 20 *m/s* equals a Reynolds number of 13.5 *million*. Below this value, cavitation will not be of significant importance.

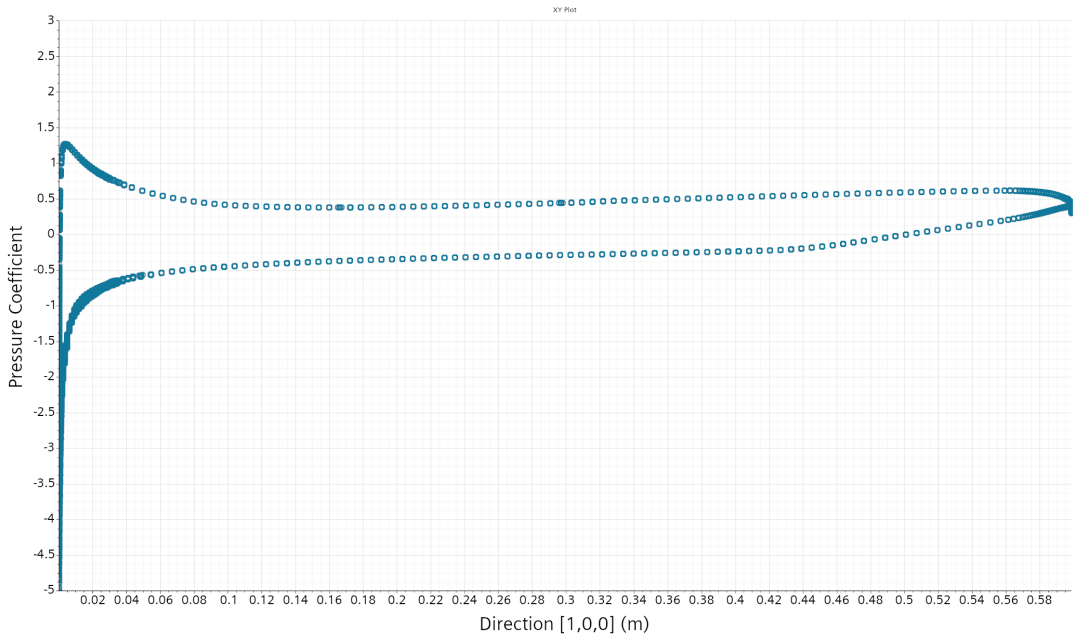

Figure 3.17: Pressure coefficient distribution x/c for *Eppler 818*

3.3.4 Reynolds sweep

Two sweeps for different AOA were performed. Each sweep was divided into two test cases with the first ranging from 0.5 *m/s* to 12.5 *m/s* at 3 *m/s* intervals, and the second ranging from 2 *m/s* to 50 *m/s* at 16 *m/s* intervals. This covers Reynolds numbers from $33.67 \cdot 10^4$ to $33.67 \cdot 10^6$. The profile tested was the *Eppler 818* with an AOA of 4 *degrees*, results are shown in Section 4.1.

3.4 Numerical analysis of free surface effects on lift and drag

To validate if the findings from previous studies [6][9][8] regarding lift and drag for different submergence depths are valid for higher Reynolds numbers, a new study on free surface effects was performed.

A mesh refinement for the free surface was already implemented from Section 3.3. Submergence depths from 4 to 0.4 h/c were simulated since depths deeper than two chord lengths showed to have very little influence from the surface in previous studies, and 0.4 since shallower depth could result in wave breaking, which would introduce uncertainty to the results. The same setup was used for the free surface study as for the Reynolds convergence study. This was made possible due to the configuration of the simulation in the previous study. The simulation had been tailored to meet the requirements of both studies.

4

Results

The findings of the research conducted in this project are presented in this chapter. The results, along with the theoretical study, form the foundation for the discussion and conclusions drawn in chapter 5.

4.1 Reynolds dependencies

Computed C_L and C_D are visualized in Figure 4.1a, Figure 4.1b, and Figure 4.2. The result shows that lift converges towards a constant value with a higher Reynolds number. The first test point, which correlates to a Reynolds number of 340.000 gives a lift coefficient of 3.7, which is unfeasible for this hydrofoil at this AOA.

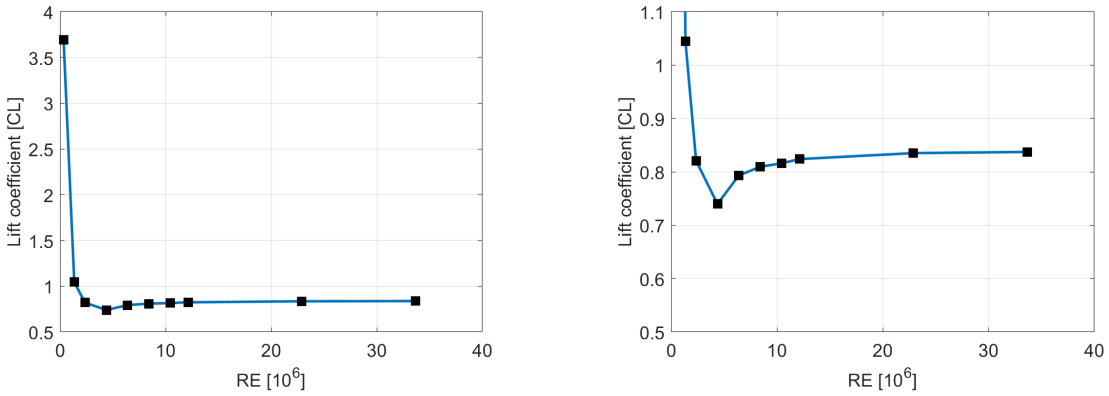

(a) C_L for Re sweep **(b)** Zoomed view of C_L for Re sweep

Figure 4.1: C_L for Reynolds number sweep

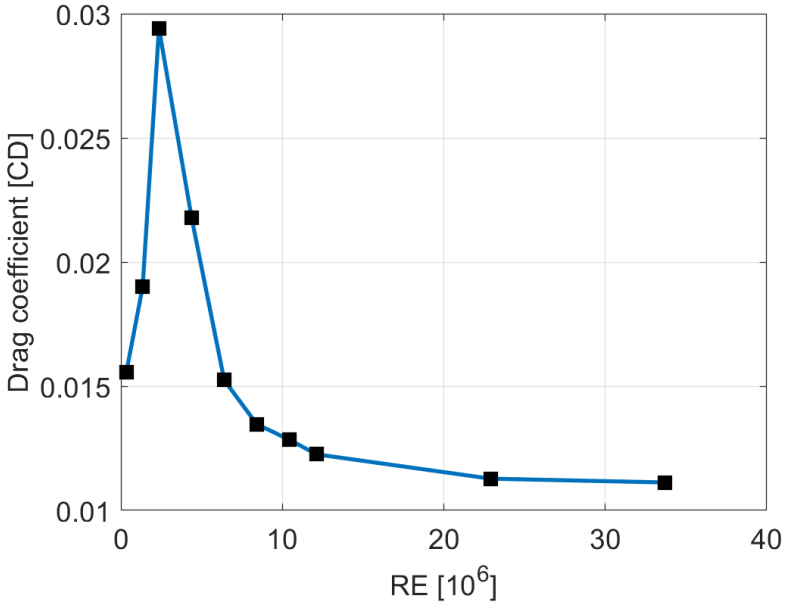

Figure 4.2: Drag coefficient for varying Reynolds number

It can be observed that the lift decreases up to a Reynolds number of 4.4 *million* and then increases again toward a value of 0.83 at a Reynolds of 33 *million*. The percentage disparity between the C_L and C_D for each point and the final value of 33 *million* is presented in the Table 4.1 and 4.2.

Table 4.1: Percentage disparity for C_L between final value and each point

Re [10^6]	C_L	Percentage disparity [%]
0.34	3.694	341.15
1.347	1.050	24.80
2.357	0.820	2.00
4.378	0.740	11.64
6.4	0.793	5.25
8.4	0.809	3.33
10.4	0.816	2.53
12.1	0.823	1.60
22.9	0.835	0.26

Table 4.2: Percentage disparity for C_D between final value and each point

Re $[10^6]$	C_D	Percentage disparity [%]
0.34	0.0156	39.81
1.347	0.0190	70.80
2.357	0.0294	164.41
4.378	0.0218	95.88
6.4	0.0152	37.04
8.4	0.0135	21.07
10.4	0.0128	15.45
12.1	0.0126	10.17
22.9	0.0113	1.37

The vector velocities contour plots with skin friction on the hydrofoil surface are plotted to understand the phenomena leading to this behavior. Three key aspects are examined. Firstly, in the boundary layer development, the boundary layer gets thinner with an increased Reynolds number as seen in Figure 4.3. At a certain Reynolds number, the boundary layer thickness stabilizes, and lift begins to converge. This can also be observed by looking at the skin friction on the wing, which is closely linked to the boundary layer. At high Reynolds numbers, large skin friction is primarily confined to the region near the leading edge. The skin friction rapidly decreases due to the fast development of the boundary layer. Secondly, the transition between laminar and turbulent flow. Looking at the area close to the leading edge an area of low skin friction can be observed, which entails that the flow is laminar at this stage. This phenomenon is illustrated in Figure 4.3b, which has a large area of laminar flow, equivalent to the blue area. Increasing the Reynolds number gradually decreases the laminar zone, and at 12 *million*, it has almost disappeared, see Figure 4.3e. This entails that the flow is fully turbulent. Lastly, the separation on the hydrofoil. For all test points, except for the first one which has the lowest Reynolds, separation is not present. At the first test point, separation occurs both at the leading and trailing edges, see Figure 4.4, leading to significant errors and uncertainties in the simulations.

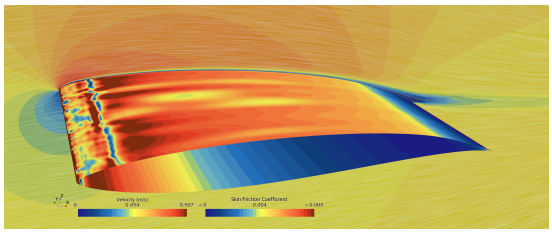

(a) Re=0.34 *millions*

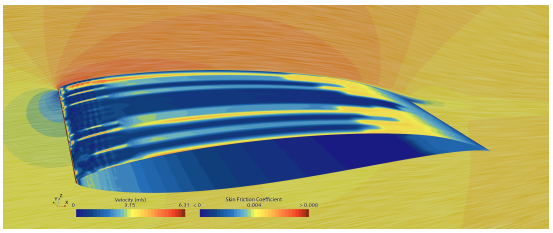

(b) Re=2.36 *millions*

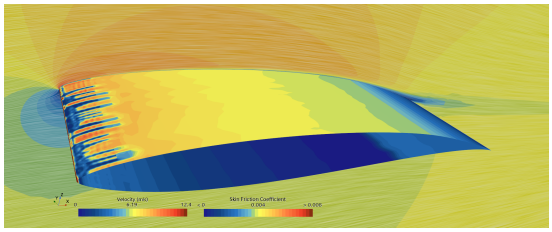

(c) Re=4.38 *millions*

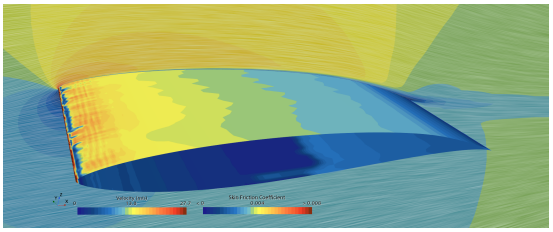

(d) Re=8.42 *millions*

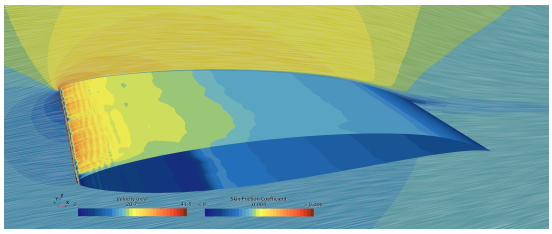

(e) Re=12.12 *millions*

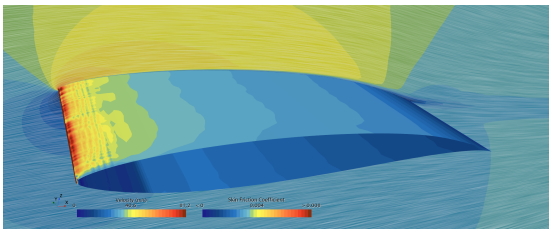

(f) Re=22.90 *millions*

Figure 4.3: Figures (a-f): velocity contour in the free-stream and skin friction on the hydrofoil surface to visualize boundary layer development for Reynolds sweep.

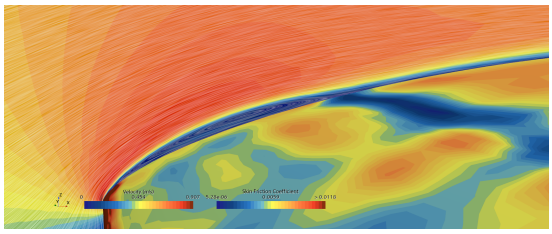

(a) Vector field for leading edge

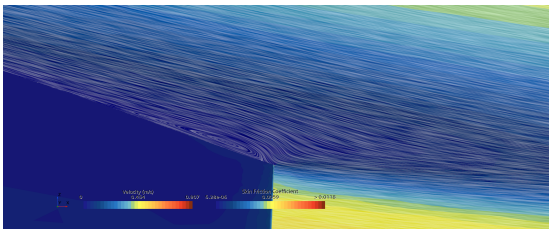

(b) Vector field for trailing edge

Figure 4.4: Laminar separation at Re=340.000

4.2 Free surface effects

Results from the free surface study, visualized in Figure 4.5, show a constant decrease in lift as submergence depth is decreased from h/c=4 to h/c=0.4 for Re = 6.4 *million*. The drag, from h/c=4 to h/c=2, is shown to increase for decreased submergence depth. From h/c=2 to h/c=0.4, the drag instead decreases.

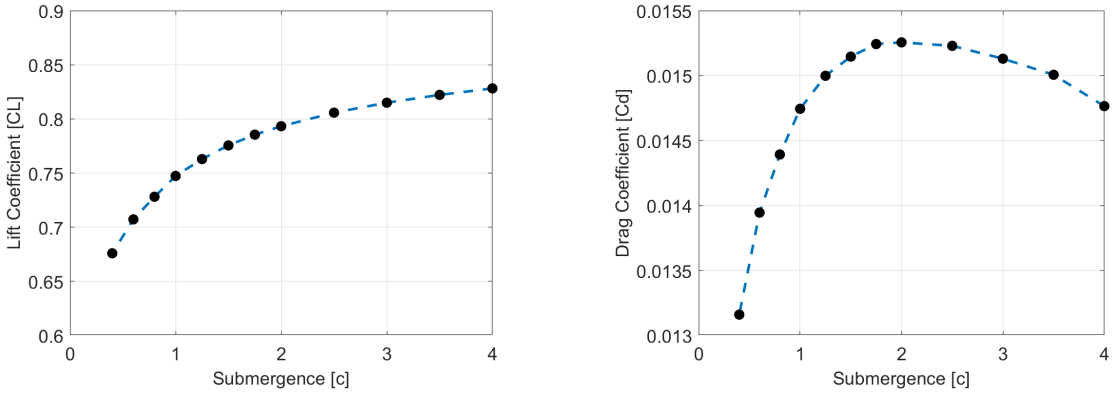

(a) C_L **(b)** C_D

Figure 4.5: Lift and drag for different submergence depths

Extracting and investigating pressure fields for the depths 0.4c, 1c, 2c, and 4c as seen in Figure 4.6, the low pressure above the foil is much more distinct at deeper submergence than what is seen closer to the free surface. This is also shown in Figure 4.7, where the hydrodynamic pressure is presented for 0.4c submergence and 4c submergence. It can be observed that the hydrodynamic pressure difference increases with deeper submergence. Looking at the velocity contour in Figure 4.8, this can be explained by the free stream velocity above the hydrofoil being lower at 0.4c than at 4c.

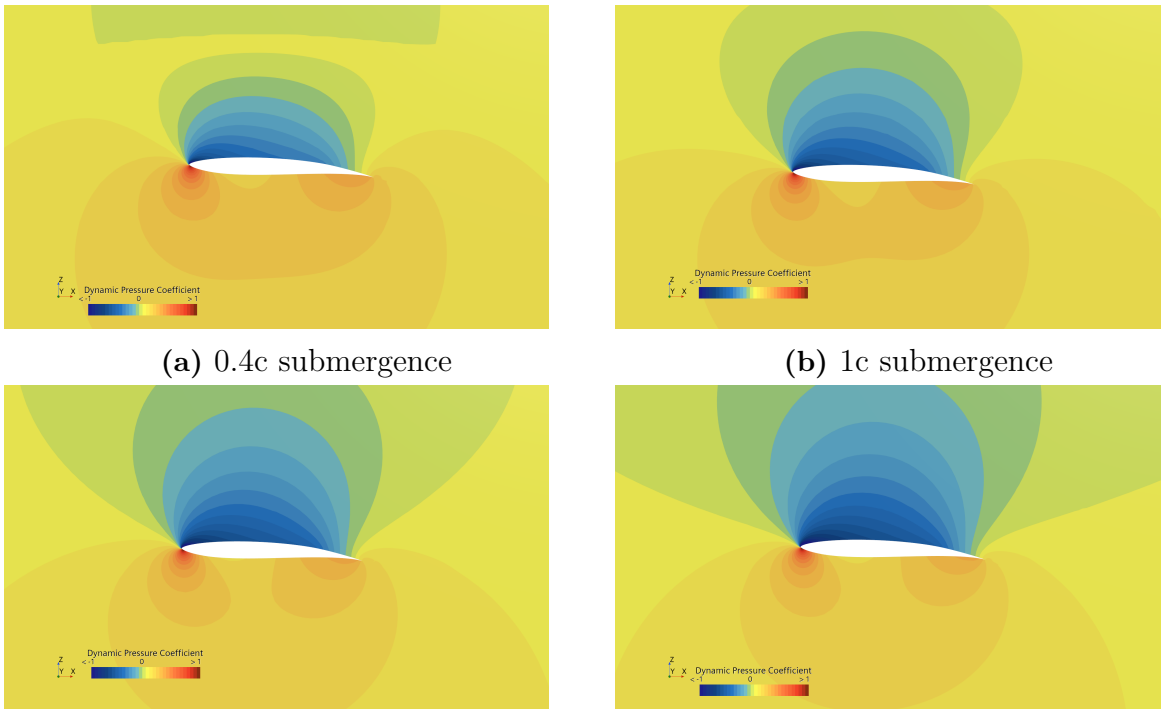

(a) 0.4c submergence **(b)** 1c submergence

(c) 2c submergence **(d)** 4c submergence

Figure 4.6: Hydrodynamic pressure coefficient for different submergence, Re=6.4*million*

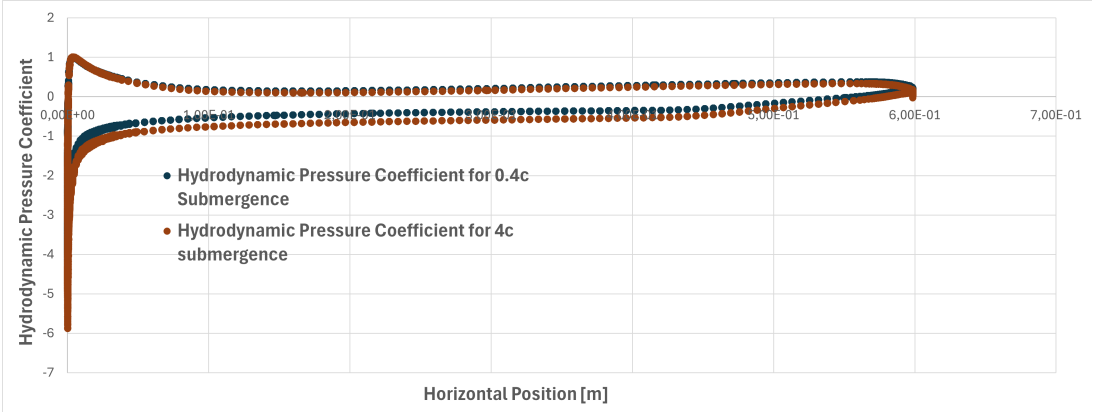

Figure 4.7: Hydrodynamic pressure for 0.4c and 4c submergence , Re=6.4*million*

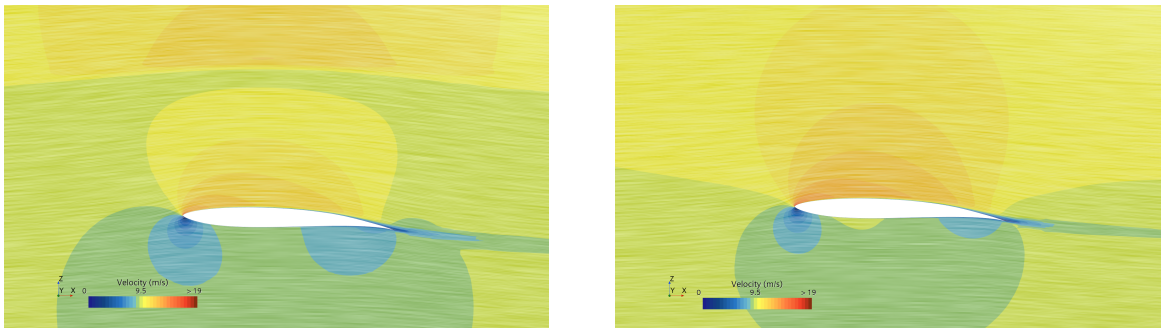

(a) Velocity at 0.4c submergence **(b)** Velocity at 4c submergence

Figure 4.8: Flow velocity around hydrofoil for different submergence, Re=6.4*million*

The wave height for different submergence depths is shown in Figure 4.9. It can be observed that the wave height above the hydrofoils increases as the hydrofoil operates closer to the surface. Both the Reynolds number and the Froude number are the same and only the depth base Froude number is changed, thereby keeping a constant wave period.

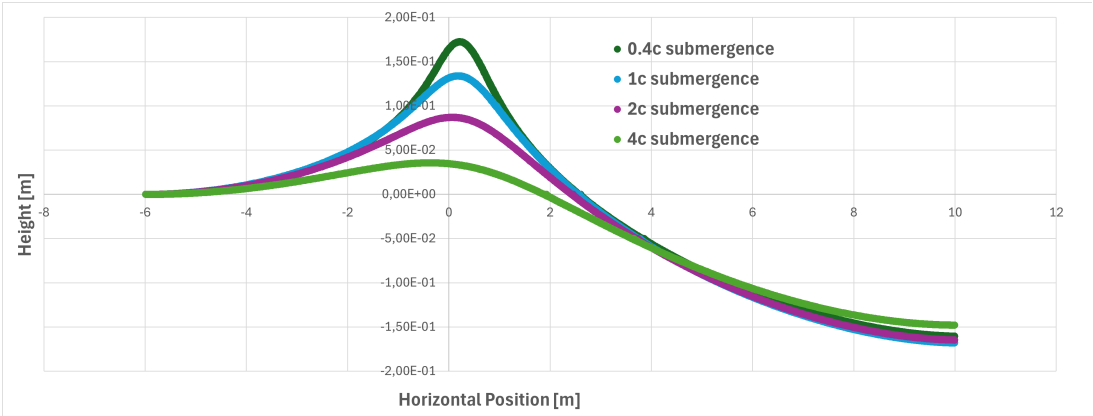

Figure 4.9: Wave height for different submergence depths, Re=6.4*million*

The streamlines for different submergence depths are presented in Figure 4.10. It can be

observed that the flow changes direction due to closer proximity to the free surface. For the deeper submergence, a flatter flow can be seen compared to shallower submergence.

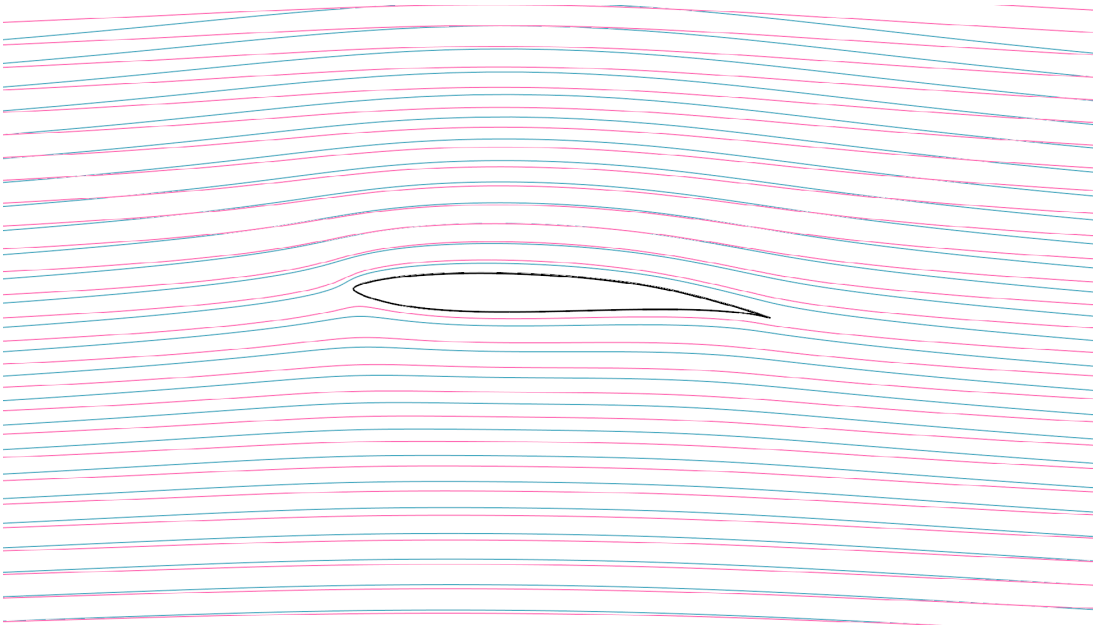

Figure 4.10: Streamlines comparison for different submergence, Re=6.4*million*, Blue=0.4c, Red=4c

5

Discussion

5.1 Reynolds Convergence

The lift and drag converge at a relatively high Reynolds number, as shown in section 4.1. Therefore, scaling the Reynolds number without corrections is not possible for most Reynolds numbers. Depending on the acceptable percentage disparities, convergence occurs at different Reynolds numbers. If 5 % is set to be an acceptable error, all tests above a Reynolds number of approximately 6.5 *million* would result in the same lift and approximately 18 *million* for drag. Most of the hydrofoils used today operate under these Reynolds numbers. To account for this, a correction factor could be used, similar to the form factor that is being used for displacement vessels today.

At this stage, with only one profile tested it is not possible to conclude that all profiles will follow the same behavior. More tests have to be conducted to form a database. With the collected data, a correction factor for different profiles could be developed. This could be done by running a Reynolds number sweep for different profiles where the thickness and camber are varied to find any correlation between them. If a correction factor could be developed, tests in a towing tank would be possible for most cases.

Two aspects that have to be investigated are transition and separation. Transition will be an issue for lower Reynolds numbers, but it will still be in a reasonable range for testing. If a hydrofoil operates in a fully turbulent flow, the test should be conducted in similar flow conditions. If the speed of the towing tank is restricted, the hydrofoil size has to be increased to ensure the test Reynolds number is above the transition, or other methods such as flow tripping or applying roughness on the leading edge can be used for forcing the laminar to turbulence transition. Secondly, separation will also be of importance. As discussed in the results inaccuracy will be larger when separation is present, which will affect the correction factor.

5.2 Free surface effects

The lift and drag results for various submergence ratios exhibit differences from both previous studies and the findings of this work. *Karim et al.* [6] observed a sharp decline in lift as h/c<1 for Fn = 0.5711, while *Andersson and Granli* [10] reported a significantly increased lift for h/c=0.5 compared to h/c=2 at Fn = 0.4. Conversely, our study reveals a consistent reduction in lift for lower submergence ratios at Fn = 3.9137. This suggests that factors beyond the submergence ratio alone influence the determination of lift and drag coefficients at different heights. Upon closer examination of the Froude number and wave profiles together with lift and drag data, similarities begin to emerge. From Figure 4.6a the flow is seen to be diffused by the wave, which is further discussed below.

5.2.1 Diffusion and compression

The surface of the wave functions as a barrier, guiding the flow according to its contours. The wave generated by the foil can serve as either a converging nozzle, where it compresses and accelerates the flow by narrowing the gap between the free surface and the foil, or as a diverging nozzle, diffusing the flow, slowing it down, by expanding the area between the free surface and the foil. The configuration of the wave shape dictates its influence on lift, which is not solely reliant on submergence.

Subcritical flow

For subcritical flow, i.e. when $Fn < 1$, it has been shown that a wave trough is formed above or slightly behind the upper, low-pressure side of the foil. This wave trough acts as a duct that decreases the area and accelerates the flow, similar to the Venturi effect. As the flow accelerates, its pressure decreases due to Bernoulli's principle, contributing to higher lift generation on the foil. In other words, the formation of the wave trough acts as a natural Venturi duct, accelerating the flow and lowering the pressure above the foil.

Supercritical flow

For supercritical flow, i.e. $Fn > 1$, a bow shock is formed upstream of the foil, initiating a wave that has its crest just above the foil. This crest diffuses the flow between the free surface and the foil, slowing it down and generating a lower pressure difference between the upper and lower sides of the foil. Consequently, the lift generation is lower.

Looking at the following plot from *Andersson and Granl* [10] Figure 5.1, wave profiles for both subcritical and supercritical conditions are shown.

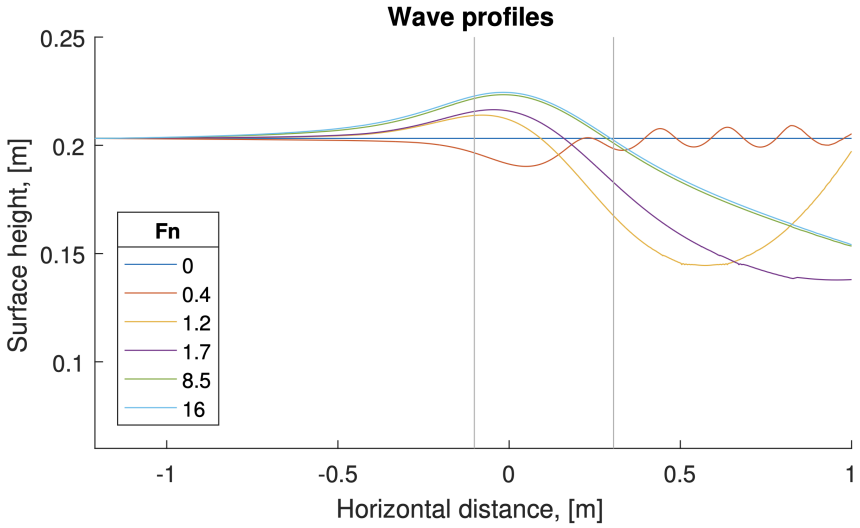

Figure 5.1: Waveprofiles for different Fn, Andersson and Granl [10]

Wave elevation for different Fn plotted on a longitudinal cut. The grey vertical lines show the leading and trailing edge of the foil respectively. Between the grey lines, a wave trough can be seen for the subcritical flow state Fn=0.4, and a wave crest is seen for all the other, supercritical flow states.

Another explanation for why the lift is reduced closer to the free surface could be that the flow aligns differently around the foil due to the wave for different submergence ratios and thus changes the effective AOA, as shown in Figure 4.10. These findings are consistent with the work of *Andersson and Granl*[10], who demonstrated the dependence of lift and drag on submergence depths.

For $Fn > 1$, the lift increases with deeper submergence, as shown in Figure 4.5. One reason for this behavior could be the presence of transition. As shown in section 4.1, C_D and C_L have not fully converged at Re = 6.4 *million* which means that transition might occur at this point. Transition will affect the lift and drag of the hydrofoil. For higher Reynolds numbers a flatter lift curve at deeper submergence is expected due to the absence of transition.

5.3 Wave scaling

The ideal scenario of having chord-based Froude number and Reynolds number matching is not possible. The Reynolds sweep showed flow similarities for a range of Reynolds numbers and thus, lift and drag coefficients can be extrapolated. Geometrical wave scaling can only be achieved by matching the Froude number, Fn. The testing depth should then follow the geometrical scaling of the hydrofoil.

5.4 Case evaluation

Experimental tests are restricted by several limiting factors as described in Section 2.4.1. Depending on the geometrical size of the foil, operational speed, and loading on the wing, the foil can either be tested in its full size or scaled while parameters such as velocity and submergence are adjusted.

The process can be explained with a flowchart, illustrated in Figure 5.2

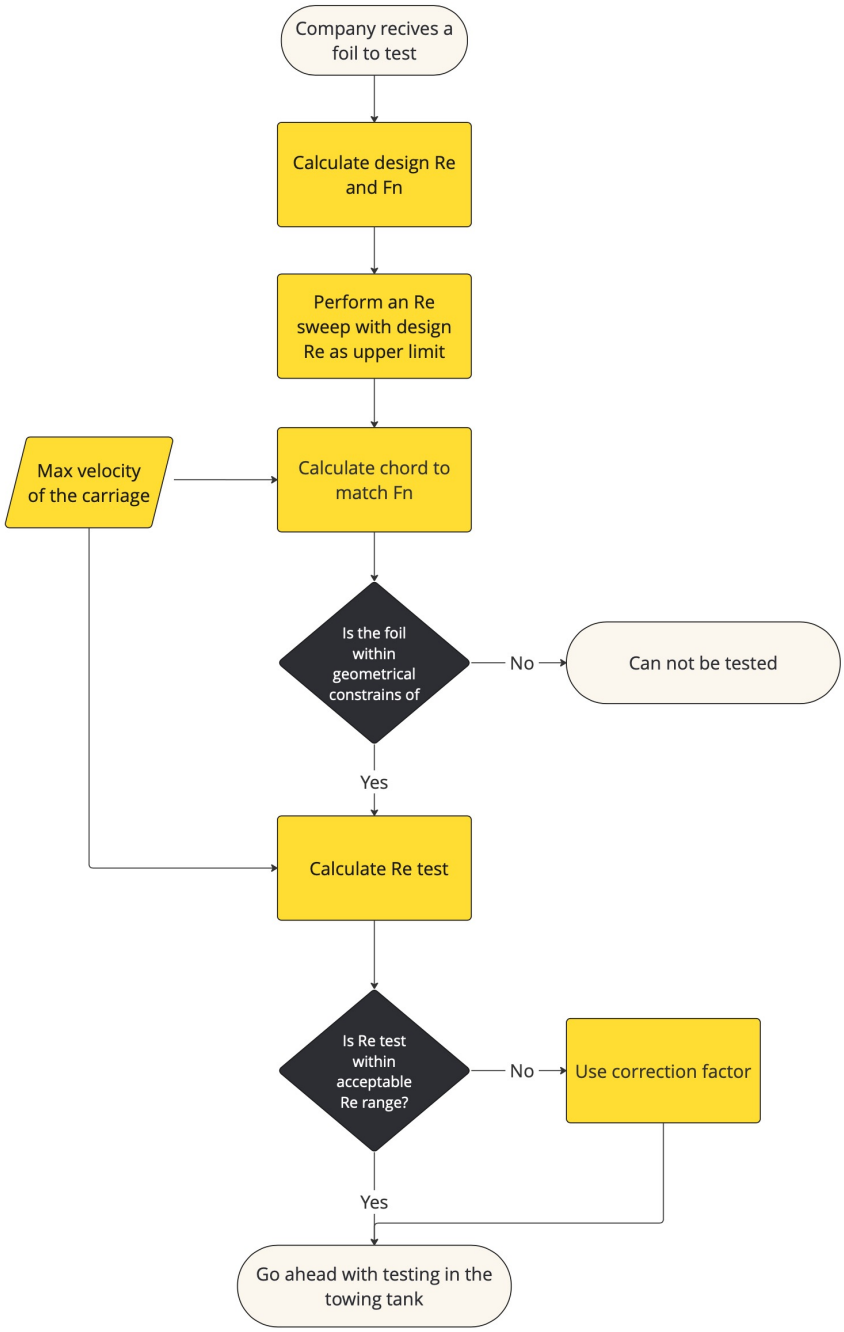

Figure 5.2: Flowchart to test a foil in the towing tank

A full-size foil can be tested if:

- The foil is within the geometrical limits for the towing tank
- Re_{test} is within the acceptable range, corresponding to a similar flow state between operation and testing conditions.
- Lift force is below the maximum load limit of the carriage.

5.5 Example

To give an example, consider the following scenario: a full-size foil with a chord length of 0.2 *meters*, operating at a submergence depth h/c=2 at a speed of 25 *kn* is to be tested in the towing tank. The foil is within the geometrical limits of the towing tank and could be tested in its full scale. From Equation 2.9 Re is calculated to 2.5 *million* and from 2.7 Fn is calculated to 9.18. The maximum testing speed is constrained by the load capacity of the carriage, but can never exceed $10m/s$. To obtain geometrical wave scaling, Fn_{test} needs to match Fn, thus $Fn_{test} = Fn$. A new chord c_{test} is calculated based on max carriage speed:

$$c_{test} = (\frac{v}{Fn})^2/g = 0.12m \tag{5.1}$$

The corresponding Re_{test} becomes 1.4 *million* (2.9). A scale factor (s) can be established: $s = c_{test}/c = 0.12/0.2 = 0.6$. This scale factor is then used to calculate the test depth: $h_{test} = h\cdot = 0.2 \cdot 0.6 = 0.12m$. This way the wave is geometrically scaled between the operational and testing conditions.

As described in section 5.1, a Reynolds number above 6.5 *million* is necessary to maintain the correct C_L, which is well above the Re_{test} in this example. Therefore a correction factor has to be used. The test Reynolds number is equal to 1.4 *million* and to match the 2.5 *million* that the real hydrofoil operates in a correction factor for C_L of 0.79 should be used. This was calculated by dividing the C_L at Reynolds 2.5 *million*, which is equal to approximately 0.81, and dividing by 1.03, which is C_L for Reynolds equal to 1.4 *million*. With this suggested method, the measured C_L at a Reynolds number of 1.4 *million* from the towing tank should be corrected by 0.79 to get the correct C_L.

6

Conclusion

This report has made an attempt to tackle the problem of model-scale testing hydrofoils in controlled environments by investigating and examining flow phenomena in *CFD*. A verification and validation study was carried out on experimental data to investigate appropriate solver settings to be used in later simulations. The verification involved a mesh convergence study and investigation of different turbulence models. To be able to match real-life conditions, including the water surface a new domain was set up. The *k-ω SST* turbulence model with *Gamma-ReTheta* transition together with the *Volume of Fluid (VOF)* model was used on an *Eppler 818* profile at 4 *degrees* AOA. With this domain, several studies were carried out including Reynolds number dependence and a submergence study.

The components of wave drag and skin friction drag should both be accounted for when testing at non-operational conditions. Due to Reynolds effects, testing a scale-down version of a foil will not be representative of the full scale foil if velocity is not increased. With limitations in the testing facility, testing at those speeds is not possible. *CFD* software is an accurate and effective tool to develop and iterate on designs before production. Today, *CFD* is considered reliable if modeled correctly but needs to be compared and tuned to experimental data. Therefore, experimental testing is suggested only to validate numerical simulations before the final product is flight-tested and put into commercial use.

To allow for testing at different Reynolds numbers, a correction factor has to be established. This could be done by performing Reynolds sweeps on different wing configurations, creating a database to identify similarities. This also becomes of importance as 3D effects can be hard to predict, such as varying chord length and profile along the span of a wing.

For Fn<1, the wavelength is short and lift increases with decrease in submergence, due to the flow between the surface and foil being compressed and accelerated.

For Fn>1, the wavelength is long and lift decreases as submergence depth decreases, due to the flow between surface and foil being diffused and redirected.

Suggested testing depths as found in some reports, usually around 1.5c to 2c, should be negated for some instances. Depending on the Froude number different wave patterns will occur and therefore different lift and drag characteristics. If the Froude number is less than 1 the suggested high of 1.5c to 2c is a balanced operation height. But for a Froude number larger than 1, different lift and drag characteristics are found, lift increases with increase in submergence depth. Which entails that the foil should operate deeper than 1.5c-2c when only looking at a horizontal foil. In reality, a horizontal hydrofoil can not work by itself, a vertical strut is always present and introduces frictional resistance.

The test height for a model-scale hydrofoil should be scaled with the same factor as the

chord length, which is decided through Froude number similarities from full scale to model scale. This is necessary to keep geometrical similarities.

Lastly, this report focused on developing a method to test a horizontal foil only, with respective operating depth. In real life, a vertical strut holding the horizontal foil will give rise to drastically increased drag as submergence is increased due to a larger wetted area. Designing a foil requires careful consideration to include the effects of both horizontal and vertical foil as a system.

6.1 Future work

Model-scale testing can be favorable for different reasons. In this report, emphasis has been put on measuring drag and lift coefficients by using a static model of a foil. Experimental tests are needed to validate the results of this work.

Another important aspect to test in model scale is the maneuvering characteristics and dynamics of the foils. While static testing is easy to control and analyze, it has limitations in investigating flight dynamics. A dynamically scaled model is a free-going platform that captures the dynamic of the full-size model. The Reynolds effects could be solved by changing the profile of the foil to match the characteristic of lift and moment curves for the full-size model[2]. Further studies could be done with a special focus on dynamic scaling. It may not be necessary to have the resistance and dynamics completely coupled. The engine of a radio-controlled model scale boat, operated at low Reynolds numbers could be scaled independently to compensate for the proportionally increased or decreased drag.

Further investigation on free surface effects for high Froude numbers is necessary to be able to understand the correlation between them. As presented in this thesis, a higher Froude number leads to a longer wave period. For very high Froude numbers the wave period will go towards infinity, resulting in a flat free surface. In that case, different submergence would allegedly have no impact on the lift. If and when this happens should be investigated to conclude if wave scaling for model scale tests could be neglected.

Bibliography

[1] *29th International Towing Tank Conference*. Vol. Volume II. 2021.

[2] Gavin K. Ananda et al. "Design Methodology for a Dynamically-Scaled General Aviation Aircraft". In: *35th AIAA Applied Aerodynamics Conference*. DOI: 10.2514/6.2017-4077. eprint: https://arc.aiaa.org/doi/pdf/10.2514/6.2017-4077. URL: https://arc.aiaa.org/doi/abs/10.2514/6.2017-4077.

[3] De Tavernier D.A.M. "Aerodynamic advances in vertical-axis wind turbines De". In: *Delft University of Technology* (2021). URL: 10.4233/uuid:7086f01f-28e7-4e1b-bf97-bb3e38dd22b9.

[4] C. Johansson. "Transition modelling in Simcenter STAR-CCM+". In: *Volupe* (May 13, 2024). URL: https://volupe.se/transition-modelling-in-simcenter-star-ccm/.

[5] C. Johansson. "Y+ calculator". In: *Volupe* (May 13, 2024). URL: https://volupe.se/wall-y-calculator-when-meshing-a-geometry-for-cfd-analysis-this-handy-volupe-calculator-computes-the-height-of-the-first-mesh-cell-off-the-wall-required-to-achieve-a-desired-y-using-flat-plate-boun/.

[6] Md. Mashud Karim, Bijoy Prasad, and Nasif Rahman. "Numerical simulation of free surface water wave for the flow around NACA 0015 hydrofoil using the volume of fluid (VOF) method". In: *Ocean Engineering* 78 (2014), pp. 89–94. ISSN: 0029-8018. DOI: 10.1016/j.oceaneng.2013.12.013. URL: https://www.sciencedirect.com/science/article/pii/S0029801813004502.

[7] Mohammad Moonesun et al. "Practical scaling method for underwater hydrodynamic model test of submarine". In: *Journal of the Korean Society of Marine Engineering* 38 (Dec. 2014), pp. 1217–1224. DOI: 10.5916/jkosme.2014.38.10.1217.

[8] Zao Ni, Manhar Dhanak, and Tsung-chow Su. "Performance of a hydrofoil operating close to a free surface over a range of angles of attack". In: *International Journal of Naval Architecture and Ocean Engineering* 13 (2021). ISSN: 2092-6782. DOI: 10.1016/j.ijnaoe.2020.11.002. URL: https://www.sciencedirect.com/science/article/pii/S2092678220300509.

[9] Laetitia Pernod et al. "Free-Surface Effects on Two-Dimensional Hydrofoils by RANS-VOF Simulations". In: Mar. 2022. DOI: 10.5957/CSYS-2022-012.

[10] Simon Granli Rasmus Andersson. *Free Surface Effects on Horizontal Hydrofoils*. 2018. URL: https://hdl.handle.net/20.500.12380/256126.

[11] SIMENS. "K-Omega Model".

[12] SIMSCALE. *K-Epsilon Turbulence Models*. Tech. rep. 2023. URL: https://www.simscale.com/docs/simulation-setup/global-settings/k-epsilon/.

[13] SIMSCALE. *K-Omega Turbulence Models*. Tech. rep. 2023. URL: https://www.simscale.com/docs/simulation-setup/global-settings/k-omega-sst/.

[14] Philippe R. Spalart and Christopher L. Rumsey. *Effective Inflow Conditions for Turbulence Models in Aerodynamic Calculations*. 2007. DOI: 10.2514/1.29373.

[15] Sverre Steen. "Lecture notes: Experimental Methods in Marine Hydrodynamics". In: *Faculty of Engineering Science and Technology – NTNU Trondheim, Norwegian* (2014).

DEPARTMENT OF Mechanics and Maritime Sciences
CHALMERS UNIVERSITY OF TECHNOLOGY
Gothenburg, Sweden
www.chalmers.se

CHALMERS
UNIVERSITY OF TECHNOLOGY